The significance of the melt-pond scheme in a CMIP6 global climate model

Diamond, R., Schroeder, D. ORCID: https://orcid.org/0000-0003-2351-4306, Sime, L. C., Ridley, J. and Feltham, D. ORCID: https://orcid.org/0000-0003-2289-014X (2024) The significance of the melt-pond scheme in a CMIP6 global climate model. Journal of Climate, 37 (1). pp. 249-268. ISSN 1520-0442 doi: 10.1175/jcli-d-22-0902.1 Available at https://centaur.reading.ac.uk/114042/

It is advisable to refer to the publisher's version if you intend to cite from the work. See Guidance on citing.

To link to this article DOI: http://dx.doi.org/10.1175/jcli-d-22-0902.1

www.reading.ac.uk/centaur

CentAUR

Central Archive at the University of Reading

Reading's research outputs online

The Significance of the Melt-Pond Scheme in a CMIP6 Global Climate Model

RACHEL DIAMOND,[a,b] DAVID SCHROEDER,[c] LOUISE C. SIME,[a] JEFF RIDLEY,[d] AND DANNY FELTHAM[c]

[a] *British Antarctic Survey, Cambridge, United Kingdom*
[b] *Department of Earth Sciences, University of Cambridge, Cambridge, United Kingdom*
[c] *Centre for Polar Observation and Modelling, Department of Meteorology, University of Reading, Reading, United Kingdom*
[d] *Met Office, Exeter, United Kingdom*

ABSTRACT: The impact of melt ponds on sea ice albedo has been observed and documented. In general circulation models, ponds are now accounted for through indirect diagnostic treatments ("implicit" schemes) or prognostic melt-pond parameterizations ("explicit" schemes). However, there has been a lack of studies showing the impacts of these schemes on simulated Arctic climate. We focus here on rectifying this using the general circulation model HadGEM3, one of the few models with a detailed explicit pond scheme. We identify the impact of melt ponds on the sea ice and climate, and associated ice–ocean–atmosphere interactions. We run a set of constant forcing simulations for three different periods and show, for the first time, that using mechanistically different pond schemes can lead to very significantly different sea ice and climate states. Under near-future conditions, an implicit scheme never yields an ice-free summer Arctic, while an explicit scheme yields an ice-free Arctic in 35% of years and raises autumn Arctic air temperatures by 5° to 8°C. We find that impacts on climate and sea ice depend on the ice state: under near-future and last-interglacial conditions, the thin sea ice is very sensitive to pond formation and parameterization, whereas during the preindustrial period the thicker sea ice is less sensitive to the pond scheme choice. Both of these two commonly used parameterizations of sea ice albedo yield similar results under preindustrial conditions but in warmer climates lead to very different Arctic sea ice and ocean and atmospheric temperatures. Thus, changes to physical parameterizations in the sea ice model can have large impacts on simulated sea ice, ocean, and atmosphere.

SIGNIFICANCE STATEMENT: This study investigates the impacts of melt ponds on Arctic sea ice under different climate conditions, using the HadGEM3-GC3.1-LL general circulation model (GCM). Additionally, we study the impact of changing the type of pond scheme used. We find that changing the pond scheme causes large differences to how a GCM simulates Arctic sea ice, the ocean, and the atmosphere, for both near-future and warmer paleoclimate conditions. These large differences have not been found previously, because this is one of the first GCM studies of this type. Our results demonstrate the importance of melt ponds, and their wider impacts on ocean and atmosphere. Furthermore, they suggest that better evaluation of the representation of sea ice processes is vital for the robust projection of future climate change.

KEYWORDS: Atmosphere; Ocean; Sea ice; Sensitivity studies; General circulation models

---

1. Introduction

The ongoing rapid loss of Arctic sea ice has far-reaching consequences, including rising Arctic temperatures and changes to atmospheric and ocean circulation, global climate, and weather (Pithan and Mauritsen 2014; Notz and Stroeve 2016; Vihma 2014; Sévellec et al. 2017). These changes are likely to have wide-ranging impacts on the global community and biosphere (Post et al. 2013; Jackson et al. 2015; Vihma 2014). General circulation models (GCMs) disagree by decades on the first date of an ice-free summer Arctic (Guarino et al. 2020; Docquier and Koenigk 2021; Jahn et al. 2016; Massonnet et al. 2012), where an ice-free Arctic is defined as sea ice extent < 1 million km², and models that simulate present-day sea ice conditions accurately tend to do so by simulating greater-than-observed warming (Rosenblum and Eisenman 2017; Notz and SIMIP Community 2020).

There is debate as to how much the modeling of sea ice processes within a GCM affects the simulated historical and present-day ice state, as well as the projected rate of sea ice decline: for example, some previous GCM studies have suggested that CO_2 emissions and global-mean air temperature linearly drive the annual mean of the decline of Arctic sea ice extent, with little dependence of this decline on the representation of sea ice processes within the model (Notz and Stroeve 2016, 2018; Jahn et al. 2016; Rosenblum and Eisenman 2017). Other studies suggest that the way sea ice processes are modeled strongly impacts the response of the ice to external forcings (e.g., Tsamados et al. 2015; Curry et al. 1995; Bailey et al. 2020).

It is well known that melt ponds have strong impacts on the mass and energy balance of sea ice (Perovich et al. 2002a,b). Melt ponds are systems of pools, formed from melted snow and ice, that collect on the Arctic sea ice surface from spring to summer (Perovich et al. 2002b; Perovich and Tucker 1997). Since pond-covered ice has a lower albedo than bare ice or snow, and ponds can cover up to 60% of summer sea ice, ponds amplify the ice-albedo feedbacks that lead to summer ice melt (Rösel and Kaleschke 2012; Eicken et al. 2004; Perovich and Tucker 1997; Curry et al. 1995): pond-covered ice melts 2–3 times faster than bare ice (Fetterer and Untersteiner 1998).

In GCMs from phase 6 of the Coupled Model Intercomparison Project (CMIP6), melt-pond processes are most commonly parameterized by reducing the ice and snow albedo when surface ice temperatures approach 0°C (e.g., Collins et al. 2006; Curry et al. 2001). This indirect, diagnostic treatment of ponds is termed an "implicit" pond scheme (Pedersen et al. 2009; Hunke et al. 2013). Implicit schemes have been relatively successful for reproducing realistic present-day melt rates (Collins et al. 2006; Curry et al. 2001). However, pond formation is affected by sea ice processes throughout melt season (e.g., evolving topography and snow cover), which this implicit scheme type does not represent (Flocco et al. 2012; Hunke et al. 2013). Furthermore, as Arctic sea ice continues to thin, sea ice will likely become increasingly sensitive to pond formation and melting (Schröder et al. 2014). For these reasons, there has been increasing focus during the last 15 years on incorporating more detailed prognostic melt-pond models (termed "explicit" schemes) into GCMs (Taylor and Feltham 2004; Lüthje et al. 2006; Skyllingstad et al. 2009; Scott and Feltham 2010; Flocco et al. 2012; Hunke et al. 2013). Implicit schemes are more commonly used in CMIP6 models: of the 125 CMIP6 model configurations, 14 use an explicit melt pond scheme (11%) and the remaining 111 use implicit treatments (from https://wcrp-cmip.github.io/CMIP6_CVs/docs/CMIP6_source_id.html).

Despite this progress on the explicit representation of melt ponds, studies of the climate implications of these explicit pond schemes have been relatively limited. They tend to fall into two broad categories, namely studies of (i) the sensitivity to pond scheme in standalone sea ice models, and/or sea ice models coupled to a simple slab or mixed-layer ocean (Tsamados et al. 2015; Sterlin et al. 2021; Flocco et al. 2010, 2012; Uotila et al. 2012; Hunke et al. 2013), or (ii) the impacts of pond formation by removing, or fully deactivating, the pond scheme in GCMs (Roeckner et al. 2012; Holland et al. 2012). We are aware of just one study, by Pedersen et al. (2009), that investigated the impacts on sea ice in a GCM of altering the pond scheme. This used physically simpler pond schemes than the topographical models available today, which resulted in the authors showing only small ice thickness and concentration differences when the pond scheme was altered.

Pond-scheme studies in standalone sea ice models suggest relatively small impacts on simulated sea ice of changing the pond scheme (Flocco et al. 2012). Pond formation studies in GCMs show that pond formation has significant impacts for sea ice and Arctic climate year-round: pond formation leads to amplified albedo feedback, increased summer sea ice melt,

increased ocean–atmosphere heat flux in autumn, and faster ice regrowth (Holland et al. 2012). Sources of uncertainty arising from the parameterization of sea ice processes, particularly those relating to melt ponds (Roach et al. 2018; Rae et al. 2014), thus clearly require further study, particularly ascertaining how modern parameterizations of melt ponds may impact projections of climate change.

This study's aim is to address the knowledge gap and determine, under different climate conditions, (i) the absolute contribution of melt ponds to sea ice melt, and ocean and atmospheric temperatures; and (ii) the necessity of using a detailed melt-pond model to reliably simulate Arctic sea ice and climate. The primary impact of melt ponds on the sea ice is via amplification of the albedo feedback in the shortwave range. Diamond et al. (2021) show that ponds had a significant impact during the Last Interglacial period (LIG), from 130 to 116 thousand years ago when Arctic summer top-of-atmosphere shortwave radiation was 60–75 W m^{-2} greater than the preindustrial period (PI). Met Office GCM HadGEM3-GC3.1-LL (henceforth simply HadGEM3) is equipped with a comprehensive topographical pond scheme in its sea ice component CICE5.1 (Hunke et al. 2015), so we apply this model to study the impacts of pond formation.

HadGEM3, one of the only GCMs with this scheme implemented, simulated no summer sea ice during the LIG (Kageyama et al. 2021; Guarino et al. 2020) and had high climate sensitivity (Andrews et al. 2019; Meehl et al. 2020). Although HadGEM3's high sensitivity is largely due to strong cloud feedbacks (see, e.g., Andrews et al. 2019), it is clear from a comparison with the previous version of the model (HadGEM2-ES) that the shortwave albedo feedback is also ~1.5 times as strong in the newer version of the model (Flynn and Mauritsen 2020). Therefore, here, we investigated the impact of changes to the albedo parameterization directly.

We investigate ocean–ice–atmosphere interactions related to melt-pond processes, and the impact on Arctic climate of melt-pond formation during three climate periods: (i) the preindustrial (PI), (ii) the LIG, and (iii) near-future conditions. For each climate period we run HadGEM3 with three parameterizations of melt ponds: pond scheme E, this explicit (most detailed) representation of melt ponds that is implemented in HadGEM3; pond scheme I, the simpler implicit parameterization of melt ponds outlined above; and pond scheme N, in which ponds are removed entirely.

In section 2, we outline the methods used for this study, describing the model and methods of analysis. In section 3a, we present results related to sea ice, and in section 3b we present results related to the ice–ocean–atmosphere interactions. In section 4, we conclude, put our results in context with the literature, and discuss implications of our results.

2. Methods

a. Model

All the simulations analyzed in this study use the low-resolution version of the U.K. CMIP6 physical climate model, HadGEM3-GC3.1-LL, hereinafter referred to simply as

HadGEM3 (Williams et al. 2018). HadGEM3 is a fully coupled climate model that uses the Unified Model (UM) (Walters et al. 2017) for the representation of the atmosphere, the Joint U.K. Land Environment Simulator (JULES) for the representation of land surface processes (Walters et al. 2017), and the NEMO3.6 (Madec et al. 2015) and the CICE5.1 (Hunke et al. 2015) models for the representation of the ocean and the sea ice, respectively.

In its low-resolution version (N96-ORCA1), HadGEM3 utilizes a horizontal grid spacing of approximately 135 km on a regular latitude–longitude grid for the atmosphere. For the ocean, an orthogonal curvilinear grid with a grid spacing of approximately 1° is used. For the vertical discretization, the UM atmospheric model utilizes 85 pressure levels (terrain-following hybrid height coordinates) while the NEMO ocean model uses 75 depth levels (rescaled-height coordinates).

The modifications and setup of the applied sea ice model CICE 5.1 (hereinafter referred to simply as CICE) are described in Ridley et al. (2018b). The standard elastic–viscous–plastic rheology (EVP) has been applied for ice dynamics with default CICE remapping advection algorithm and ridging schemes (Hunke et al. 2015). Ice thermodynamics are based on Bitz and Lipscomb (1999) with four ice and one snow vertical layers. A semi-implicit coupling scheme between atmosphere and sea ice has been introduced to ensure the stability of the solver (West et al. 2016). As for most sea ice models applied in GCMs, at the subgrid scale an ice thickness distribution function (ITD) describes the relative area within each grid cell that is covered by ice of a given thickness (but not the spatial distribution of ice of each thickness (i.e., the model does not explicitly represent the subgrid-scale topography). In CICE, the ITD is discretized with five thickness categories, and the dynamic and thermodynamic evolution of the sea ice is separately calculated for these five categories within each grid cell (Flocco and Feltham 2007; Flocco et al. 2010). The lower bounds for the five ice thickness categories are 0, 0.6, 1.4, 2.4, and 3.6 m, as described in Ridley et al. (2018b) and Rae et al. (2015). For full details on model configuration, performance, and improved physics relative to older model versions, see Williams et al. (2018) and Ridley et al. (2018b).

b. Pond schemes

HadGEM3 uses a four-band radiation scheme: one visible and one near-IR band, and within each of these, one diffuse and one direct band [Ridley et al. (2018b), based on the default CICE4.1 four-band radiation scheme in Hunke et al. (2010)]. The shortwave albedo scheme in HadGEM3 is split over the visible and near-IR ranges, with visible being 0.38–0.67 μm and near-IR being 0.67–1.02 μm (Ridley et al. 2018b). The albedos are calculated separately within each grid cell for each of the five ice thickness categories. For both bands, for each of ice, ponds, and snow, the direct and diffuse albedos are equal (more details provided below). We use the same parameterization of snow albedo for all schemes [i.e., the default scheme used in HadGEM3-GC3.1-LL and described in more detail in Ridley et al. (2018b)], but the way

TABLE 1. Bare ice, snow, and pond albedo values used in shortwave range in simulation. For bare ice, snow, and ponds, these albedo values are used for both direct and diffuse radiation [this is a good approximation because of the time of year of pond formation (Flocco et al. 2010)]. See the text in section 2b for further information.

Parameter	Value (visible)	Value (IR)
Ice albedo	albicev_cice: 0.78	albicei_cice: 0.36
Snow albedo	albsnowv_cice: 0.96	albsnowi_cice: 0.68
Pond albedo	albpondv_cice: 0.27	albpondi_cice: 0.07

ice and pond albedos are calculated differs between models as follows.

For the default explicit topographic pond scheme used in the sea ice component of HadGEM3, which we hereinafter denote pond scheme E, the albedo calculation is based on the scheme used in the CCSM3 model (Hunke et al. 2015) but includes surface melt ponds by applying the explicit topographic melt-pond model of Flocco et al. (2012, 2010). Pond evolution is modeled by including snowmelt contributing to spring/summer pond formation; reduced albedo of pond-covered ice; vertical drainage of ponds through ice; and ponds refreezing in autumn. In reality, pond formation occurs when meltwater, formed as a result of snowmelt, ice melt, and precipitation, runs downhill under the influence of gravity to collect on sea ice (Flocco et al. 2010). In CICE, within each grid cell, there are five ice thickness categories but ice topography is not modeled explicitly (see section 2a). Therefore, to account for pond formation, for a given grid cell, for each time step, the surface height of each thickness category is calculated. Within a grid cell, applying the continuum hypothesis yields the conclusion that meltwater in this grid cell will be transported to ice of the lowest surface height within one time step. Therefore, all meltwater present in the cell (after accounting for melting, freezing, advection, precipitation, drainage, and runoff) is distributed between the thickness categories in order of increasing surface height (Flocco et al. 2010; Flocco and Feltham 2007; Flocco et al. 2012). Provided the calculated pond height is above sea level, a prescribed fraction of this "ponded" meltwater runs into the ocean (to account for runoff around the edges of floes or through cracks); the sea ice permeability controls what proportion of the remaining meltwater drains vertically through the ice. Pond refreezing near the end of melt season is accounted for by modeling the formation of ice lids on the pond, that grow, partially melt, or melt completely, depending on the surface flux. Thus, by modeling pond formation, runoff, drainage, and refreezing for each grid cell, at each time step, the evolution of pond fraction of the sea ice, and pond depth on the sea ice, can be calculated, and used in a separate routine to calculate the area-averaged sea ice albedo (Flocco et al. 2010; Flocco and Feltham 2007; Flocco et al. 2012). Relevant surface albedo parameters applied in the model are presented in Table 1 [also in more detail in Table A1 of Ridley et al. (2018b)]. For both wave bands, for ice of thickness less than 0.3 m, the underlying ocean impacts the bare ice albedo: The bare ice albedo is reduced smoothly to the open ocean albedo (Ridley et al. 2018b).

The tabulated pond albedos are only applied in simulations with topographical pond scheme E. For ponds of depth >20 cm, this scheme uses albedo of 0.27 in the visible range and 0.07 in the near-infrared range (Ridley et al. 2018b). These albedos are significantly smaller than the albedos of ice and snow, which vary through the year in the range 0.5–0.9 and are calculated as described in Hunke et al. (2015). Ponds of depth <4 mm are assumed not to impact the albedo: the albedo of such ponded ice is equal to that of bare ice. For ponds with depths from 4 mm to 20 cm, the albedo is calculated by linearly combining the bare ice and melt pond albedos [as the underlying bare ice is assumed to impact the total pond albedo; see Ridley et al. (2018b) for further details].

Simulations run with scheme N used HadGEM3-GC3.1 as described above, but with the topographical pond scheme turned off and all meltwater drained directly to the ocean rather than collecting on the sea ice as ponds.

Simulations with pond scheme I used HadGEM3-GC3.1 as described in section 2a, with the topographical pond scheme switched off. Instead, we use a temperature-dependent parameterization of ponds, as used in the previous version of the model HadGEM3-G2.0 (Rae et al. 2015), based on the CCSM3 radiation scheme (Hunke et al. 2015). For each ice thickness category, for each grid cell, this returns a final temperature-dependent ice albedo α_{ip} that accounts for both bare and ponded ice, given by

$$\alpha_{ip} = \begin{cases} \alpha_i, & \text{if } T < T_p \\ \alpha_i + \dfrac{d\alpha_{ip}}{dT}(T - T_p), & \text{if } T_p \le T \le T_m \end{cases}. \quad (1)$$

With this scheme, the impact of ponds on albedo is accounted for by reducing the ice albedo α_{ip} from the bare ice value α_i (see Table 1) for surface temperatures above $T_p = -1.0°C$. In the range from T_p to the ice melting temperature $T_m = 0°C$, α_{ip} is reduced linearly with temperature by $d\alpha_{ip}/dT = -0.075$ per degree Celsius.

Therefore, for all three schemes, within each of the two wave bands, the final grid-box albedo $\alpha(n)$ of sea ice in each of the five thickness categories n is an area-weighted average of the albedos of ice, snow and ponds (where applicable) over this ice thickness category, as follows: for scheme E,

$$\alpha(n) = f_s(n)\alpha_s(n) + f_i(n)\alpha_i(n) + f_p(n)\alpha_p(n). \quad (2)$$

For scheme N,

$$\alpha(n) = f_s(n)\alpha_s(n) + f_i(n)\alpha_i(n). \quad (3)$$

For scheme I:

$$\alpha(n) = f_s(n)\alpha_s(n) + f_{ip}(n)\alpha_{ip}(n). \quad (4)$$

Above, α_i is bare ice albedo, α_s is snow albedo, α_p is pond albedo (applied for scheme E only), and α_{ip} is combined bare and ponded ice albedo (applied as described earlier for scheme I only). Similarly, f_p is ponded ice fraction (applied for scheme E only), f_s is snow fraction (representing surface

inhomogeneity due to windblown snow, parameterized based on snow depth; Ridley et al. 2018b), and the residual fraction of sea ice is bare ice fraction f_i (for schemes E and N), or bare and ponded ice fraction f_{ip} (applied for scheme I only). Note that here, to make the calculation of sea ice albedo clearer, f denotes "fraction of the sea ice" (e.g., for a given grid cell f_p is fraction of the sea ice area covered by ponds). In the remainder of the paper, we use this same quantity in almost all cases. For the cases in which we use area fraction of the grid cell (e.g., fraction of the grid-cell area covered by ponds), we note this redundantly.

c. Simulations

This paper analyses output from nine simulations: three climate scenarios (LIG, PI, and near-future), each with, as described in section 2b, the three different pond schemes: E, I, and N. These simulations are described in more detail below.

The preindustrial (PI) simulation with pond scheme E in this study was prepared and run by the U.K. Met Office as part of CMIP6 (Eyring et al. 2016). This simulation uses invariant solar, greenhouse gases (GHGs), ozone, tropospheric aerosol, volcanic, and land-use forcing for the year 1850 [see Menary et al. (2018) for details]. The climate system took about 615 model-years of spinup to attain a steady state. These years are not used in our analysis. Of the subsequent 500 model-years of the simulation (Menary et al. 2018), the first 200 are used here in our analysis.

The Last Interglacial (LIG) simulation with pond scheme E in this study was first presented by Guarino et al. (2020); it constitutes the U.K.'s Paleoclimate Modeling Intercomparison Project 4 (PMIP4) LIG contribution, as part of the wider CMIP6 project. The LIG experiment fully complies with the standard PMIP4 experimental protocol for Last Interglacial climate simulations, as described by Otto-Bliesner et al. (2017). In more detail, the Last Interglacial climate was forced using the constant 127 000 astronomical parameters based on Berger and Loutre (1991), and constant atmospheric trace GHG concentrations derived from ice core records [see Otto-Bliesner et al. (2017) Table 1 for full details and values used]. All other boundary conditions including ice sheets, topography, vegetation, aerosol, volcanic activity, solar constant, and so on, are identical to the PI simulation. LIG simulations with schemes N and I follow this protocol.

In addition, we aim to understand how the pond scheme affects simulated future climate. For this study, using a transient projection would require an ensemble of simulations to distinguish between the impact of natural variability and model physics. To avoid this, we perform time-slice experiments with constant external forcing. We have chosen emissions from 2014. Strictly, these simulations represent how the climate would evolve if emissions were fixed at 2014 levels for the next 100 years. In practice, these simulations represent not the current-day climate, but atmosphere, ice, and upper-ocean conditions over the next decades (Williams et al. 2018) due to the response time of climate to external forcing. The precise timing is not important for our study because we aim to investigate the impact of the pond scheme itself on a near-

future configuration of sea ice. The three near-future simulations (with pond schemes E, I, and N) are presented here for the first time. They were all initialized from the end of one of the four ensemble members that made up the CMIP6 HadGEM3 historic simulation. These simulations used the following forcings at CMIP6 2014 levels, as described in Andrews et al. (2020): CO_2, CH_4, and CFC concentrations (applied as globally invariant constants), black and organic carbon aerosols and SO_2 (applied as monthly latitude-longitude fields), and ozone (applied as a monthly three-dimensional field). All other boundary conditions were identical to those used in the PI simulation.

The four PI and LIG simulations with schemes I and N were initialized from the end of the relevant CMIP6 spinup simulation described above. For stability reasons, the LIG simulation with pond scheme I was initialized from the 10th year of the LIG simulation with pond scheme N. All simulations were at least 115 simulated years: 15 years for spinup to account for the direct response time of sea ice to changes (e.g., Bateson et al. 2022; Schröder and Connolley 2007) and 100 years for analysis.

d. Analysis

In subsequent analysis, we treat the standard HadGEM3 configuration, which uses pond scheme E, as the "control" and compare outputs from simulations with pond schemes I and N with the relevant control simulation from this time period. In this and future sections, the "I-E anomaly" denotes, for a given climate period, for a given variable, the difference between the simulation in which pond scheme I was used and the simulation in which pond scheme E was used. Similarly, the "N-E anomaly" denotes the anomaly for a given variable in simulation with pond scheme N from the relevant simulation with pond scheme E. All maps presented are computed from monthly model output, and show, for a given simulation, either 1) the time average of a variable or 2) the anomaly of the time average of a variable: this is the time average of a variable in one of the I or N simulations, with the time average of this variable in the equivalent control simulation (pond scheme E) subtracted. The statistical significance of results is assessed using Welch's two-sided t test, appropriate for comparing datasets of different lengths (Guarino et al. 2023). Unhatched regions on maps show results significant at the $p < 0.05$ level. Monthly climatologies presented were computed as the long-term mean of monthly model output. Error bars show $\pm$ the standard deviation of the monthly model output, related to interannual variability. To test whether the climatology of a given variable was significantly different between any two given simulations for a given month, Welch's two-sided t test was used to compare the two time series of this variable, for this month.

Monthly model output variables used for calculations include sea ice concentration (SIC), sea ice thickness (SIT), melt-pond fraction of grid cell, melt-pond fraction of sea ice, area of the grid cell of each ice thickness category, sea surface temperature (SST), surface air temperature (SAT), ice surface albedo, and surface fluxes: total downwelling shortwave flux, net shortwave flux downward, net longwave flux downward, net

latent heat flux upward, and net sensible heat flux upward. Shortwave albedo was calculated from total downwelling shortwave flux and net shortwave flux downward. Additionally, for each grid cell, the ocean heat content (OHC) per unit area in the mixed layer (e.g., as computed for Fig. 12) was calculated using model output variables mixed layer thickness Z and potential temperature θ. OHC was calculated as

$$\text{OHC} = \int_{z=-Z}^{0} C_P \rho \theta \, dz. \tag{5}$$

HadGEM3 uses a version of NEMO with constant heat capacity of seawater $C_P = 3991.8679$ J kg^{-1} K^{-1} (Madec et al. 2015). We assumed $\rho = \rho_0$ (accurate to $\pm 2\%$ for most ocean basins (Schmidtko et al. 2013), particularly near the surface at high latitudes), with $\rho_0 = 1026.0$ kg m^{-3} (Madec et al. 2015).

From June to September, the difference between mixed layer depth was less than 5 m between simulations in each climate period. Therefore, for all simulations within a given climate period, the mixed layer depth in simulations with pond scheme E was used for follow-up calculations.

3. Results

a. Arctic sea ice

For all three periods, as can be seen from Figs. 1a–c and 2, the mean winter (December–April) sea ice area (SIA) is similar: between 9.4 and 11.4 million km^2. For the LIG and near-future simulations (hereinafter collectively denoted as "warm-climate" simulations), winter SIA is maximum 1 million km^2 lower than in the PI simulations for all months. Summer (June to October) SIA differs greatly between all three climate periods [as discussed for the LIG and PI in Guarino et al. (2020) and Diamond et al. (2021)]. From August to September, the LIG had the lowest mean SIA (in the range 0.2–2.1 million km^2). The PI August–September SIA was in the range 5.6–7.1 million km^2. August–September SIA in near-future simulations has the largest spread: 1.0–4.7 million km^2, with ice preserved in the central Arctic and north of Greenland (see Fig. 2). From Figs. 1d–f, the PI has the largest mean sea ice volume (SIV) in all months and the LIG has the smallest, while the near-future climate has SIV intermediate between the two. As seen from online supplemental Fig. 1 (i.e., SF1; note that herein SF1–SF10 refer to the corresponding figures in the supplemental material), this is related to the PI having consistently the thickest sea ice, the LIG consistently the thinnest, and near-future conditions having ice thickness intermediate between the LIG and PI. The mean monthly melt-pond fraction of the sea ice, for all climate periods with the standard pond scheme E, is presented in Fig. 3. In the warm-climate simulations, pond formation began at the ice edge in May, and for the PI, in June. By July, almost all LIG sea ice was 45%–50% pond covered (the LIG was ice-free in August and September, so no ponds could exist). In the PI, sea ice remained through the summer, and, through July and August, was 25%–35% pond covered. At the sea ice edge, where the ice was warmer and thinner, pond coverage was larger than this, with up to 45%–50% of the ice at these latitudes covered by ponds. Under near-future conditions, the pond-covered fraction of sea
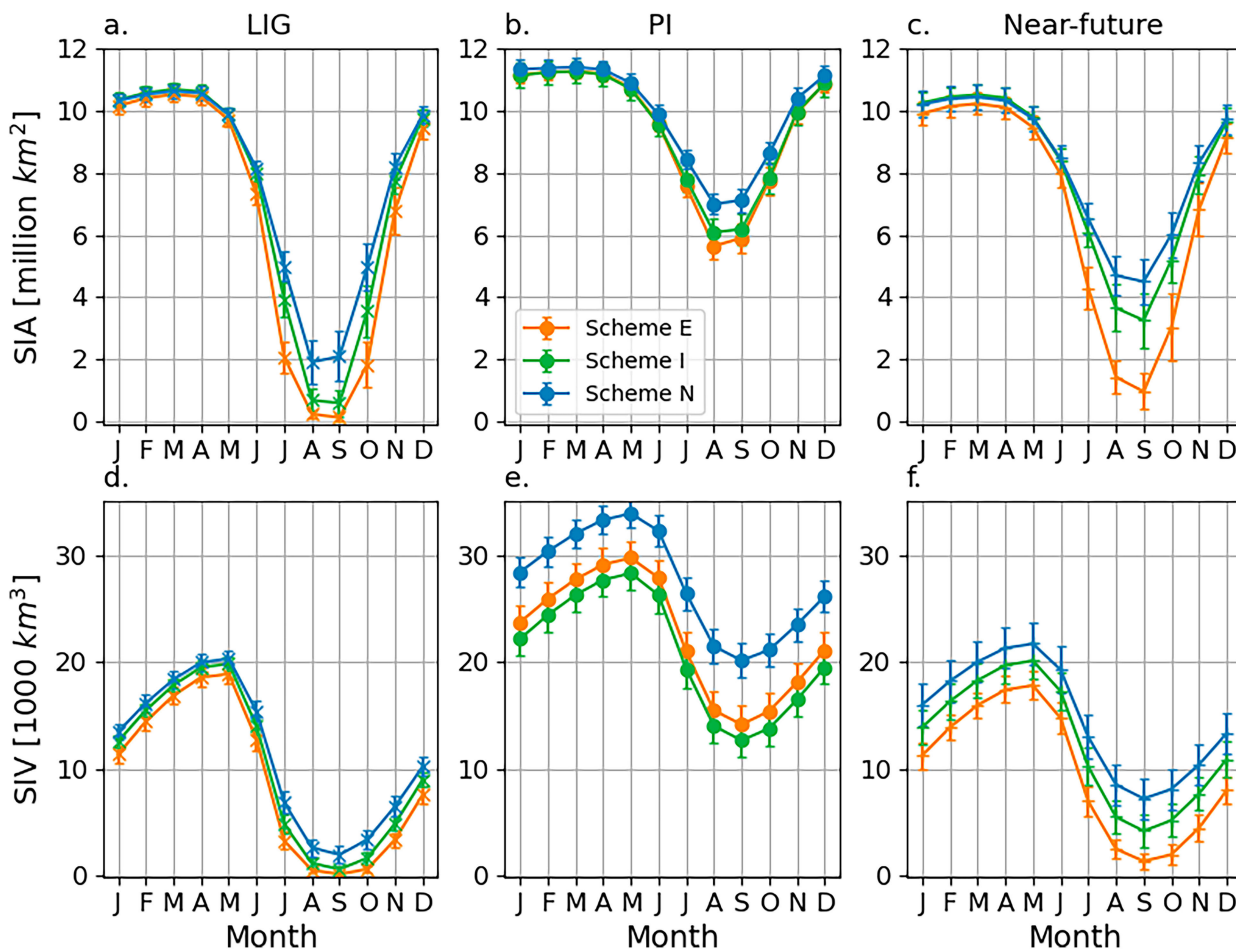
FIG. 1. Annual cycle of Arctic (a)–(c) sea ice area (SIA) and (d)–(f) sea ice volume (SIV) for the (left) LIG, (center) PI, and (right) near-future simulations The long-term mean is calculated from monthly model output over the Northern Hemisphere. Error bars show ±1 standard deviation, to represent natural variability.

ice was 40%–50% in most regions in July, falling to 25%–35% in August.

In all simulations, pond formation (i.e., using schemes I or E instead of pond scheme N) results in at least an additional 1 million km^2 of September SIE loss (Fig. 4). This is a significant increase, which can be attributed to the impact of spring and summer melt-pond formation on summer sea ice (Perovich and Tucker 1997; Perovich et al. 2002a,b; Schröder et al. 2014; Tsamados et al. 2015).

Pond schemes similar to both I and E are commonly used in GCMs (e.g., Ridley et al. 2018b; Bailey et al. 2020; Rousset et al. 2015; Wang et al. 2016), so simulations run under the same set of climate conditions, but with pond scheme E replaced by pond scheme I, may be expected to yield similar results. This holds for the PI, but not for LIG or near-future conditions. In the PI simulations, September SIE is similar between schemes I (SIE: 7.3 ± 1.1 million km^2) and E (7.2 ± 1.0 million km^2). Under "warm-climate" conditions, replacing pond scheme E with pond scheme I yields consistently greater September SIE: 0.8 million km^2 greater under LIG and 2.6 million km^2 greater under near-future conditions. Furthermore, for the LIG, using

scheme E leads to an ice-free September Arctic 98% of 100 years, whereas scheme I only leads to an ice-free Arctic for 56% of 100 years. For near-future conditions, scheme E leads to an ice-free Arctic 35% of all years, whereas scheme I never leads to an ice-free Arctic. All near-future simulations show some drift in September SIE; this is as expected given that these simulations were initialized from a transient (historical) simulation. For all climate periods, melt ponds strongly impact SIA during the summer, and SIV year-round (see Fig. 1). This can be shown by comparing, for each climate period, the simulations "with ponds" (schemes I or E) with the relevant simulation "without ponds" (scheme N). In winter: simulations with and without ponds have similar SIA, all within a range of 0.3 million km^2. Simulations with ponds have lower SIV by $1–6 \times 10^3$ km^3. In September, for the PI, simulations with ponds have lower SIA by 0.9–1.2 million km^2, and SIV by $5.9–7.4 \times 10^3$ km^3; for the LIG, simulations with ponds have lower SIA by 1.5–2.0 million km^2 (a difference of 71%–94%) and SIV by $1.3–1.8 \times 10^3$ km^3 (a difference of 67%–91%); for the near future, simulations with ponds have lower SIA by 1.3–3.5 million km^2 and SIV by $2.9–5.8 \times 10^3$ km^3.
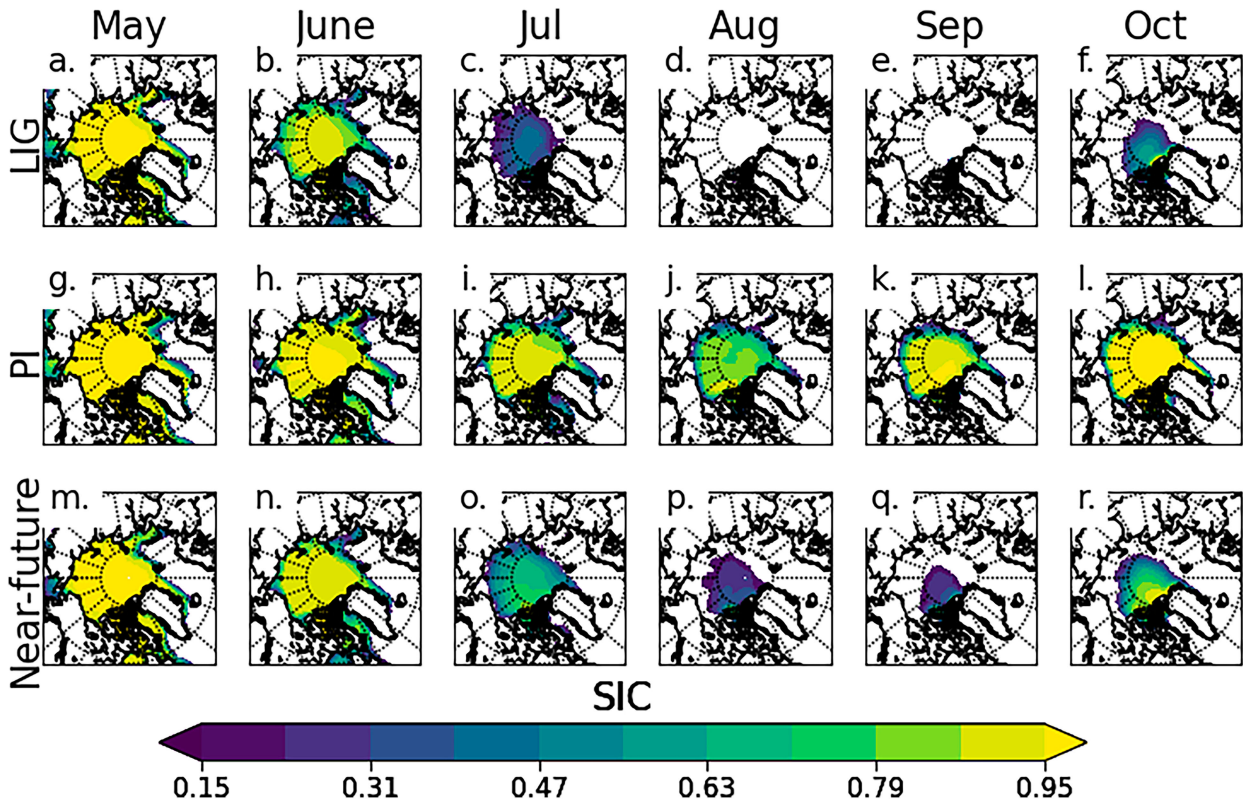
FIG. 2. Maps of the monthly long-term mean of sea ice concentration (SIC) in simulations with pond scheme E for (a)–(f) LIG, (g)–(l) PI, and (m)–(r) near-future conditions.

For all climate periods, pond scheme I, when compared with scheme E, yields greater summer SIA (Figs. 1a–c) along with greater May and June SIC at the ice edge (Fig. 5). Similar to September SIE trends, these I-E anomalies are smaller for the PI than the two warm climates.

Additionally, for the warm climates: scheme I leads to later ice loss and earlier ice regrowth. I-E SIC anomalies of 25%–45% exist in the central Arctic in July to October. Under near-future conditions, SIC I-E anomalies are largest in August and September (35%–45% in the central Arctic). For the LIG, the SIC I-E differences are 16%–30% in July and October (and only 5%–15% in August and September). This is because, in August and September, provided ponds are present (i.e., as long as schemes E or I are used), the LIG reaches a nearly (simulation I) or completely (simulation E) ice-free state (Fig. 1). Therefore, too little ice is present to allow large SIC anomalies in Fig. 5.

For all climate periods, pond formation (scheme E as compared with N) leads to thinner ice (see SF2). For the PI, using scheme I instead of E yields thinner sea ice in most regions (but thicker at the ice edge; see SF3). For the warm climates, scheme I instead of E yields thicker ice everywhere, with largest differences for the near future of up to 60 cm in August and September, and for the LIG of up to 30 cm in July and October.

From previous analysis we have learned that for both warm-climate periods, using scheme I instead of E yields significantly more summer sea ice. We now explain why these differences are larger for the near future than LIG, by investigating pond formation on each ice thickness category. As described in section 2a, sea ice evolution is separately calculated for five ice thickness categories within each grid cell. The bounds for the three thinnest categories are 0–0.6 m, 0.6–1.4 m, and 1.4–2.4 m. In near-future simulation E, from June to July, the thinnest category is almost completely (>95%) pond covered; the second-thinnest category is 60%–90% pond covered. In LIG simulation E, both the two thinnest categories are almost completely pond covered in June (very little sea ice remains in July).

From Fig. 6, for ice category 1: for all near-future simulations, SIA is similar and increases gradually from May through July due to thicker ice becoming thinner. Differences between simulations first occur in August, when this gradual increase continues with schemes I and N, but with scheme E, ice melts away faster than it is replaced. For ice category 2: differences between simulations first occur in June. Relative to June, September SIA is 91% lower for scheme E, but ~60% lower for schemes I and N. With scheme E (as outlined in the previous paragraph), ponds form almost entirely on ice categories 1 and 2: the visible range albedo is reduced for these categories from 0.78 to a minimum of 0.27 (see section 2b). Scheme I tunes the ice albedo for all categories, but only slightly (reducing the albedo from 0.78 to a minimum of 0.71). Additionally, note from Fig. 7 that using scheme E, pond-related albedo reduction begins earlier than with scheme I. With scheme E, ponds begin to form in May over most sea ice (calculated with threshold: pond fraction of grid-cell > 0.01.
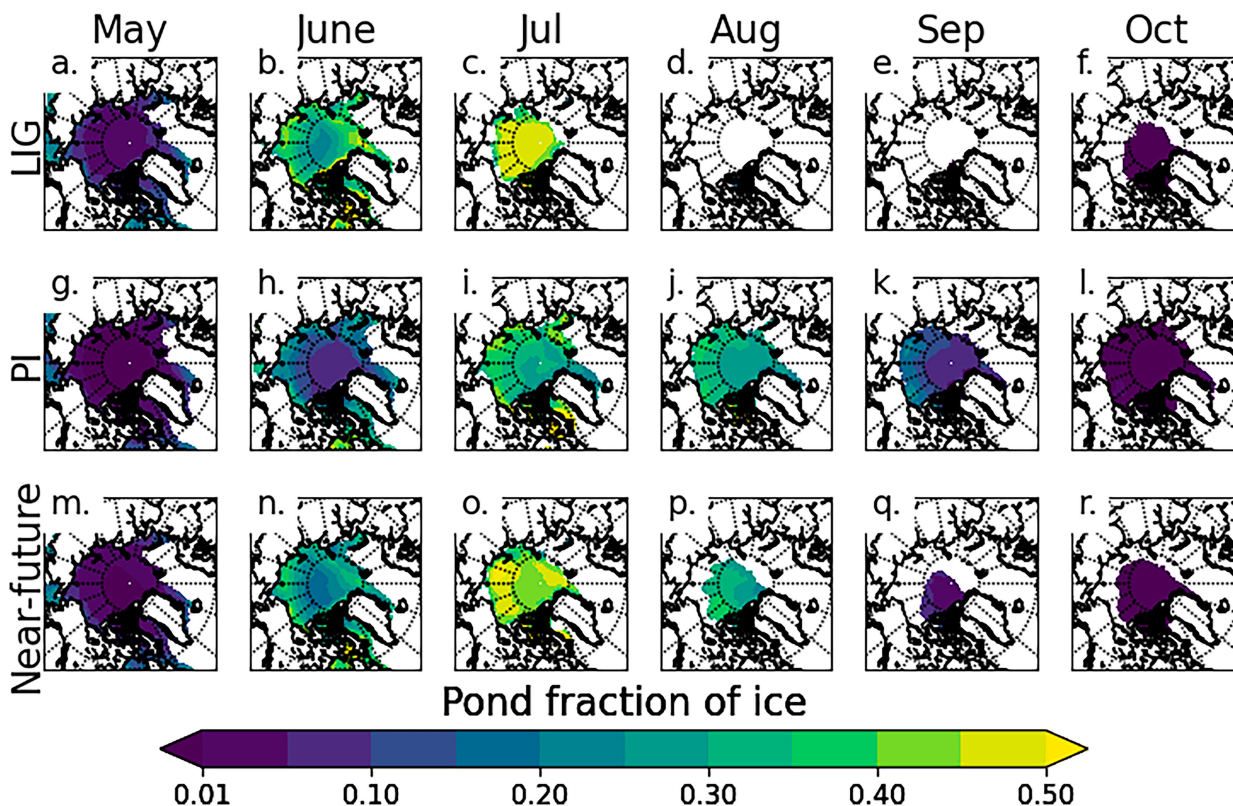
FIG. 3. Mean monthly pond-covered fraction of sea ice in simulations with pond scheme E for (a)–(f) LIG, (g)–(l) PI, and (m)–(r) near-future simulations. Only cells with mean SIC > 0.15 are shown.

Note: we use pond fraction of grid cell here, not pond fraction of sea ice, to only include cells where ponds make up a nonnegligible fraction of the area of the cell). However, using scheme I, albedo reduction begins in June (threshold: ice surface temperature $> -1°C$; see section 2b). This explains the extreme melt with pond scheme E of the two thinnest categories: these two categories have low albedo early in spring, absorb a significant amount of shortwave radiation, and melt. This exposes a large area of the ocean surface, so that secondary effects (predominantly oceanic warming likely related to albedo feedbacks, as discussed in sections 3b and 4) lead to greater melt in categories 3–5 and reduced ice volume year-round (see categories 4–5 in SF4).

For the LIG, by contrast, as seen from Figs. 6a–c, categories 1 and 2 have similar cycles no matter whether pond scheme I or E is used. The key differences are in July and October: in July, melt is delayed using pond scheme I relative to E, and in October, freeze-up begins earlier using pond scheme I relative to E (see also the comparison of timing of pond-related albedo reduction in SF5). However, for all categories, the September minima reached are similar (within 0.04–0.35 million km^2) whether pond scheme I or E is used. This is straightforward to explain: as mentioned in section 1, during the LIG, the spring and summer Arctic incoming shortwave radiation at the surface was much greater than today. This shortwave forcing (and associated ocean and atmosphere warming; see sections 3b and 4) is

large enough to melt almost all Arctic sea ice by August and September, provided ponds are represented and able to reduce ice albedo in the model (regardless of whether pond scheme I or E is used).

KEY POINTS

The differences in SIA and SIV as a consequence of pond formation (represented by the N-E anomalies for each period) are consistent between all periods: simulations with ponds (as compared with those with no pond formation) have similar winter SIA (within a range of 0.3 million km^2) and lower winter SIV (by $1-6 \times 10^3$ km^3). Simulations with ponds have considerably lower summer SIA (by 0.9–3.5 million km^2) and summer SIV (by $1.4-7.4 \times 10^3$ km^3). Summer sea ice is most strongly affected in the warm-climate simulations: for example, September SIA loss in simulations with ponds is up to 94% (2.0 million km^2) for the LIG and up to 78% (3.5 million km^2) for near-future conditions, but only 12%–17% for the PI.

Using the implicit instead of the explicit parameterization of ponds (represented by the I-E anomalies for each period) leads to statistically significant SIA differences in the summer months, and statistically significant SIV differences in all months (largest in the summer). For the PI, these SIA and SIV differences are < 15% for all months. For both warm-climate periods, these differences are considerably larger (particularly in the summer months):
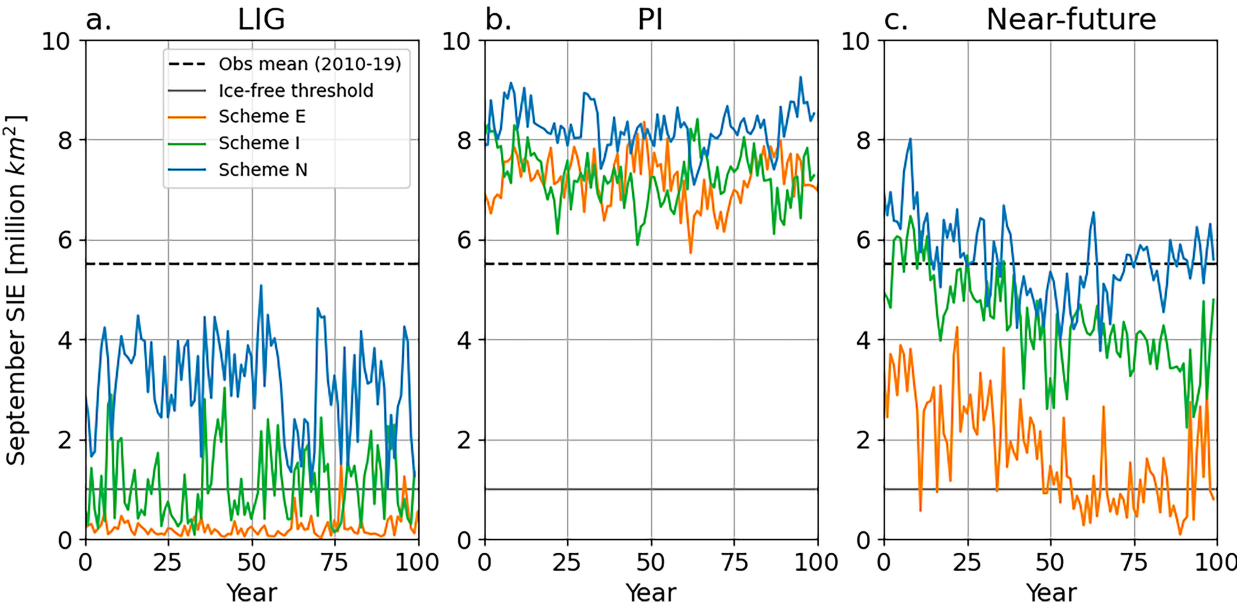
FIG. 4. First 100 years of September Arctic sea ice extent (SIE), calculated from monthly model output, using pond scheme E (orange), pond scheme I (green), pond scheme N (blue) for (a) LIG, (b) PI, and (c) near-future simulations. The horizontal dashed black line shows the 2010–19 mean for comparison, calculated from the NOAA/NSIDC sea ice concentration processed by a bootstrap algorithm, from Meier et al. (2021). The horizontal thick gray solid line shows the ice-free threshold (1 million km² of SIE).
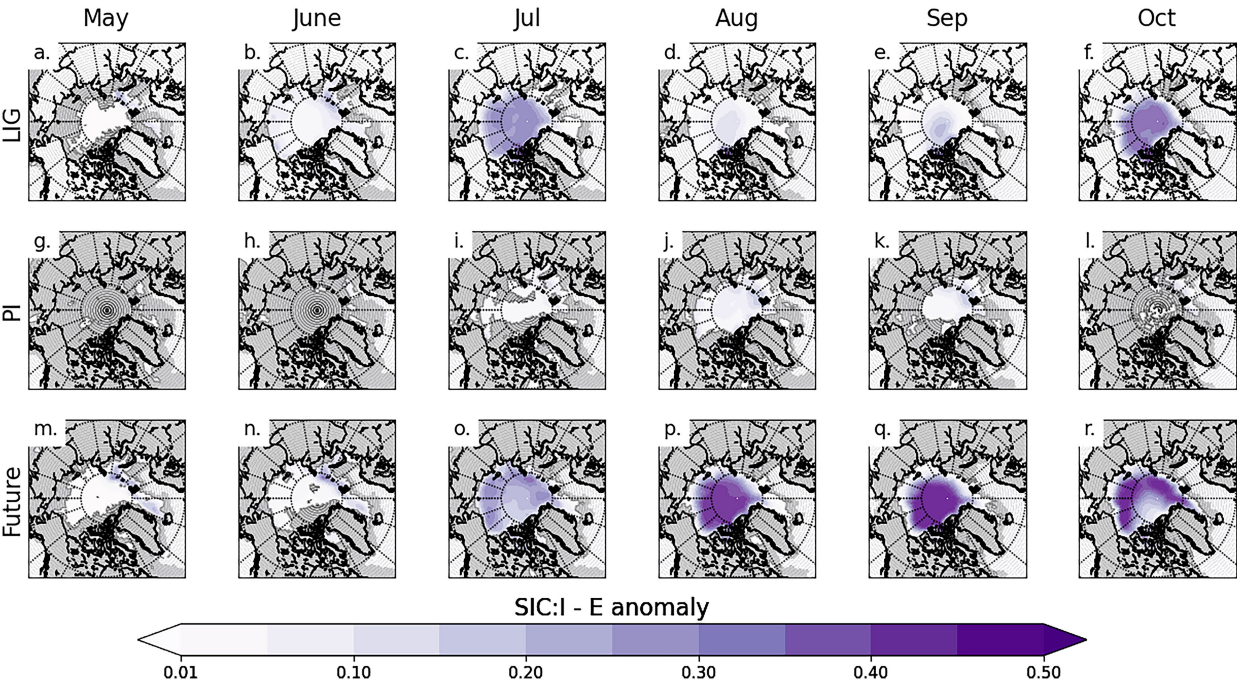

FIG. 5. Maps by month of the anomaly of the long-term mean of SIC in simulations with pond scheme I from simulations with pond scheme E for the (a)–(f) LIG, (g)–(l) PI, and (m)–(r) near-future conditions.
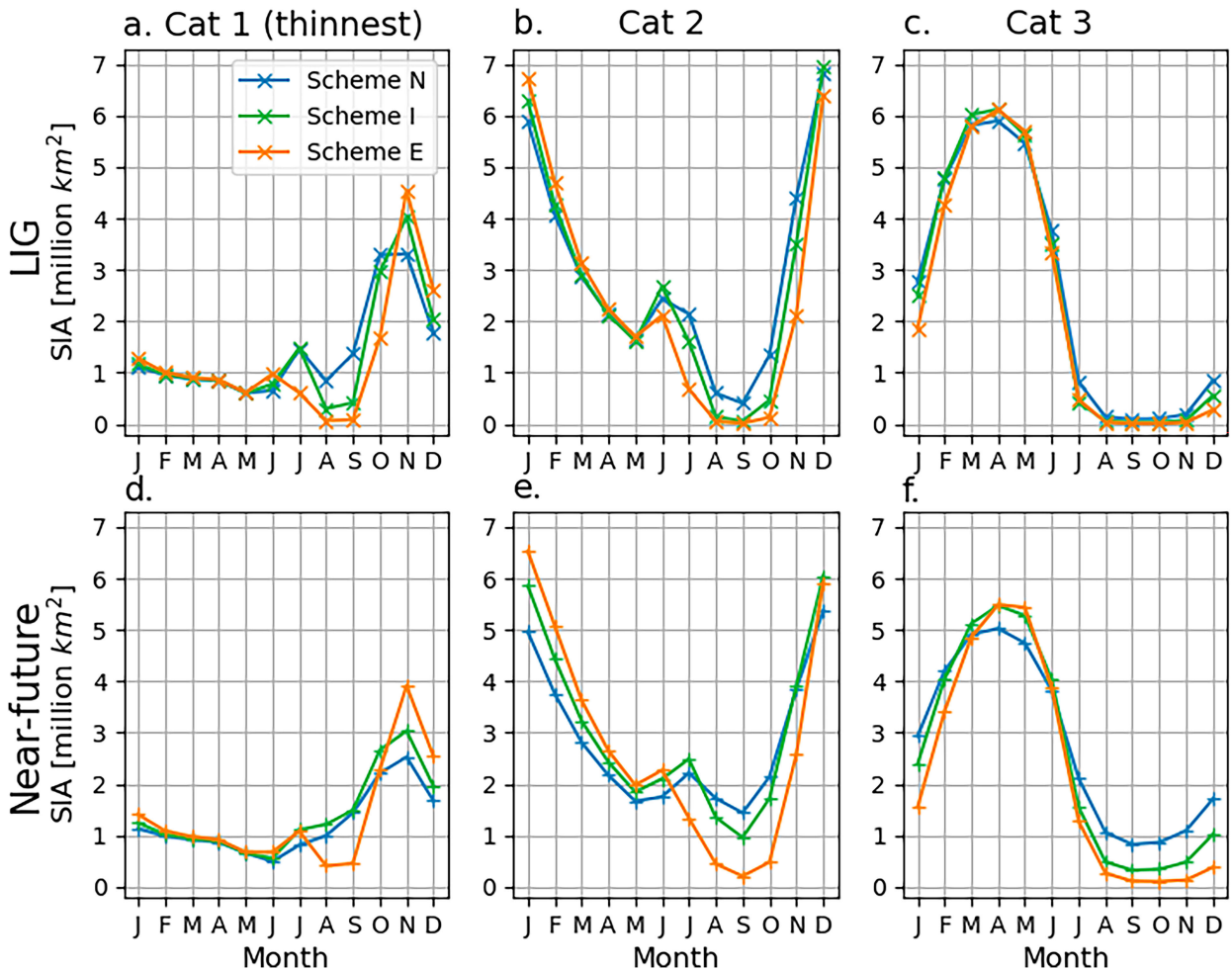
FIG. 6. Mean monthly sea ice area for the three thinnest ice categories for (a)–(c) LIG and (d)–(f) near-future conditions, showing (left) category 1 (thickness: 0–60 cm), (center) category 2 (thickness: 60 cm–1.4 m), and (right) category 3 (thickness: 1.4–2.4 m). Note in particular the SIA from May to October for categories 1 and 2.

1) For the PI: pond scheme I led to thinner ice and larger summer SIC, so overall lower September SIV (by 11%; 1.5×10^3 km^3) and higher SIA (by 5%, 0.3 million km^2).

2) For the warm-climate periods: pond scheme I led to considerably thicker ice and much greater summer SIC, and 2–4 times as great summer SIV and SIA. This corresponds to a September SIA difference of 0.5 million km^2 under LIG and 2.2 million km^2 under near-future conditions.

b. Arctic ocean and atmosphere

Through ice–ocean–atmosphere interactions, involving transfers of heat, moisture, and salt, sea ice is closely linked to surface air and sea surface temperatures (SATs and SSTs). We here investigate the impacts of melt-pond formation and parameterization on Arctic ocean and atmosphere and use anomalies of the surface energy balance and sea ice concentration to explain SAT and SST anomalies (see Figs. 8 and 9).

We show first the impact of pond formation on ocean and atmosphere, by comparing simulations with ponds (scheme E) with those without ponds (scheme N). We then show how replacing scheme E with scheme I leads to large differences in simulated ocean and atmosphere.

For all climate periods, the Arctic N-E anomaly of the summer surface energy balance shown in Fig. 9 is dominated by the shortwave component. The N-E flux anomaly reaches a magnitude for the LIG (in June) of -15.5 W m^{-2}, for the PI (in July) of -9.0 W m^{-2}, and for near-future conditions (in July) of -13.5 W m^{-2}. This is because removing ponds increases the sea ice surface albedo in May–July, which reduces the SW flux absorbed. Removing ponds reduced June top sea ice melt by atmospheric warming, and reduced July basal sea ice melt by oceanic warming (not shown): overall, less ice melted and more remained as a "barrier" between atmosphere and ocean. This reduced shortwave flux into, and heat uptake by, the upper ocean, as shown in SF6. This explains the winter to summer patterns of SST anomalies shown in Fig. 8 and SF7: the small ($<0.2°C$) winter N-E difference
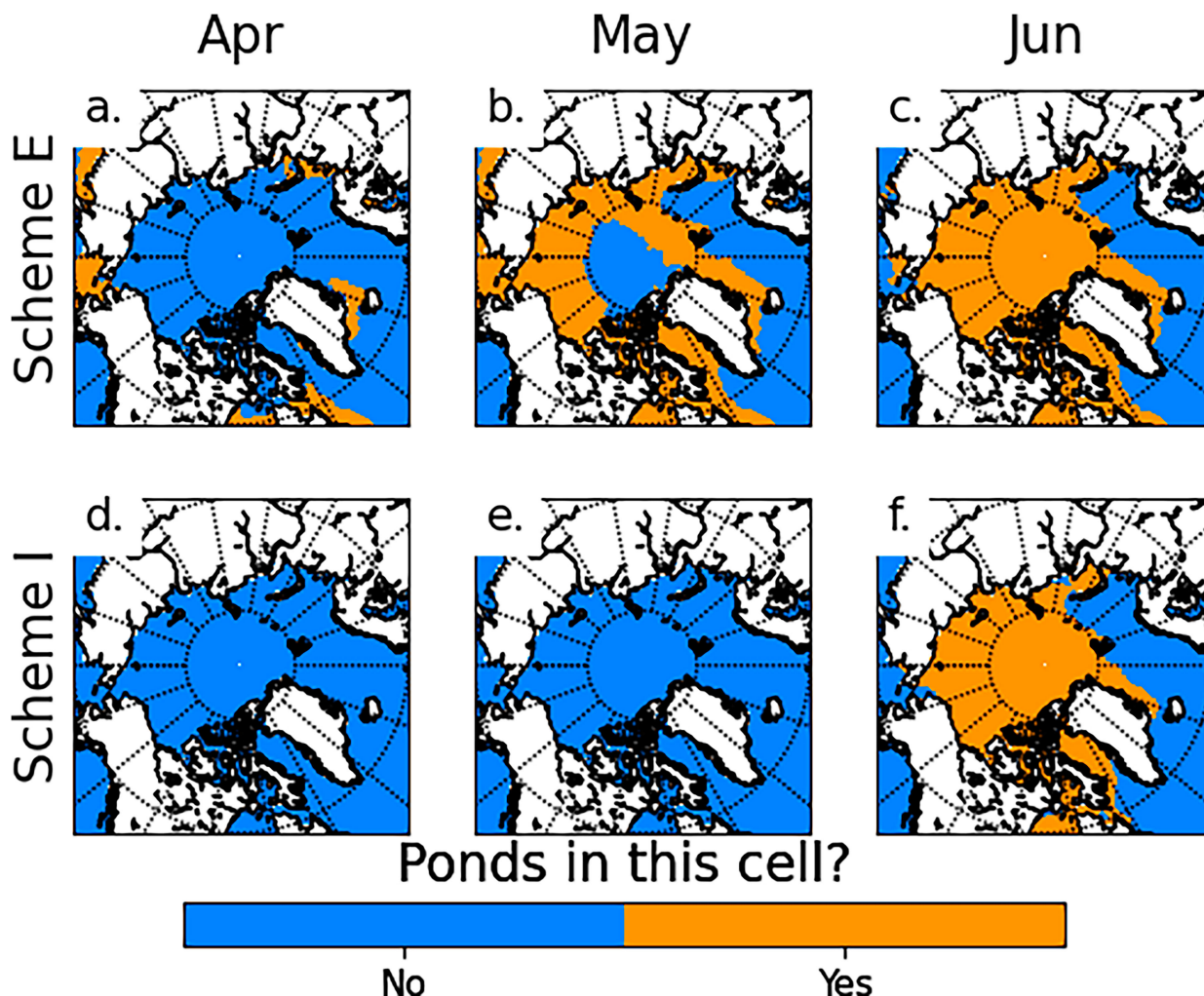
FIG. 7. For near-future simulations: maps of the mean month that pond-related albedo reduction begins in each grid cell, using (a)–(c) scheme E and (d)–(f) scheme I. The calculations are from monthly model output.

increases in magnitude through spring into summer (e.g., to nearly −1.3°C for the LIG), as the difference in ocean heat uptake between the simulations increases.

In all simulations, once incoming shortwave radiation no longer heats the Arctic Ocean surface, the ocean vents long-wave, sensible, and latent heat to the air until its surface reaches freezing temperature (see SF8) and ice can form. The positive downward N-E anomalies of total, longwave, sensible, and latent heat flux over autumn and winter shown in Fig. 9, are in real terms a negative upward flux anomaly (since fluxes of these quantities are positive upward for all simulations over autumn and winter; not shown). Therefore, removing ponds (i.e., scheme N) reduces shortwave radiation absorbed and stored as heat by the mixed layer over the summer, which leads to less heat transferred upward from ocean to air over autumn and winter, and thus lower SATs in winter. From September through February, the negative upward anomaly of heat flux (Fig. 9) reaches 6.8 W m^{-2} for the LIG, 3.0 W m^{-2} for the PI, and 7.2 W m^{-2} for near-future conditions. This heat anomaly leads to the SAT anomaly in

Fig. 8b, which decreases from ∼−0.2°C in July, to November minima of −3.0°C for LIG, −1.7°C for PI, and −3.4°C for near-future conditions. In brief: without pond formation, the ocean mixed layer absorbs and stores less heat over the summer and so, during autumn and winter, does not warm the air above it as much.

If otherwise identical simulations run with pond scheme I instead of E gave similar results, the I-E anomalies shown in Figs. 9d–f, 8b, and 8d would be near-zero. The PI I-E anomalies in Figs. 9d–f, 8b, and 8d are indeed near zero, as might be expected given that sea ice is similar between the PI simulations run with scheme I and scheme E (Figs. 1–4.) By contrast, for each warm-climate period, Figs. 9d–f, 8b, and 8d show similar (although of smaller magnitude) I-E anomalies to the respective N-E anomalies (see also maps of SATs and SSTs in SF9 and SF10). The I-E flux anomaly reaches, for the LIG (in June), −8.3 W m^{-2}, and for near-future conditions (in July), −9.1 W m^2. The summer I-E SST anomaly reaches a minimum for the LIG (in June) of −0.77°C and for near-future conditions (in July) of −0.76°C. Figure 10 shows that,
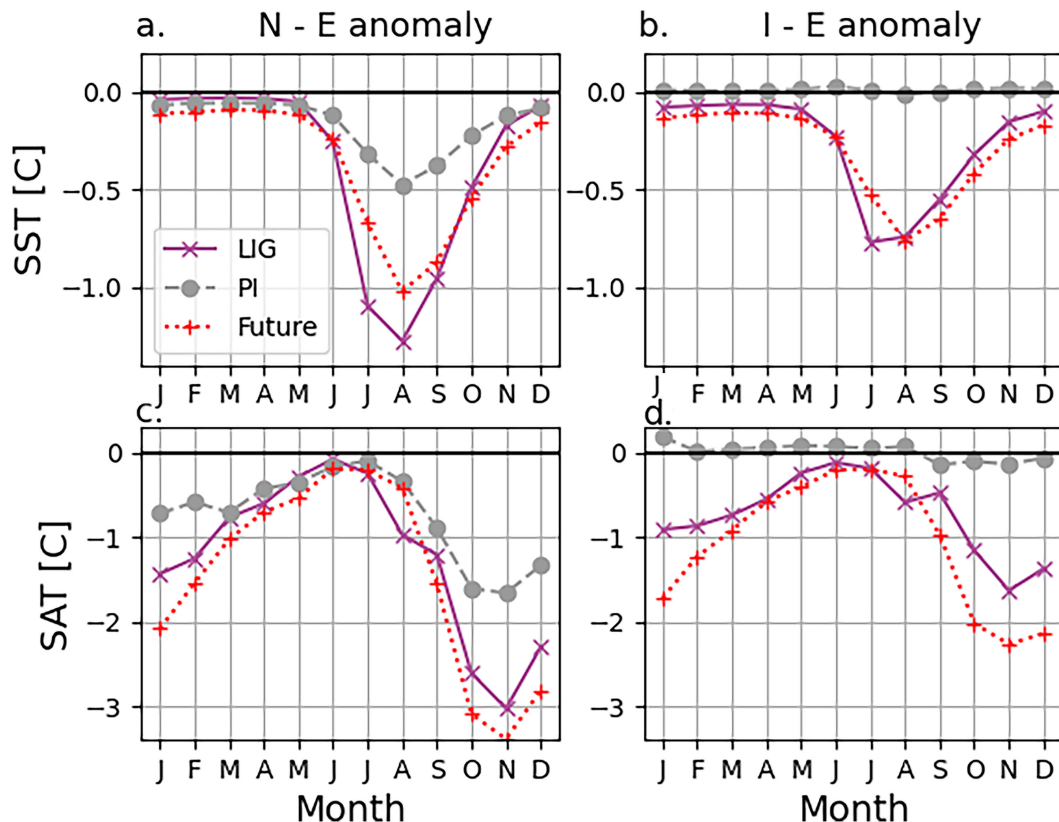
FIG. 8. Anomaly of the long-term mean of Arctic surface temperature from simulations with pond scheme E. All are calculated from monthly model output north of 66°N for the LIG (purple), PI (gray), and near-future (red) simulations. Shown are the (a) N-E anomaly of long-term mean of SST, (b) I-E anomaly of long-term mean of SST, (c) N-E anomaly of long-term mean of SAT, and (d) I-E anomaly of long-term mean of SAT. Note that (a) and (b) have different y-axis scales than (c) and (d).

under the warm climate conditions, using scheme I instead of E leads to higher spring and summer ice albedo, and reduced SW absorption. Figure 11 shows that replacing pond scheme E with pond scheme I reduces the warm-climate summer ocean heat content. We can therefore explain warm-climate I-E and N-E anomalies with the same argument.

For the PI, the SAT I-E anomaly (Fig. 8d) is near-zero (magnitude < 0.2°C) year-round. By contrast, for the warm climates, the SAT I-E anomaly decreases from approximately −0.2°C in July, to November minima of −1.6°C for the LIG, and −2.3°C for near-future conditions. Note also the particularly large SAT anomalies at high latitudes—for example, a near-future I-E anomaly of −5° to −8°C in October (see Fig. 12d and SF10). The warm-climate I-E autumn–winter SAT anomaly occurs through similar processes to the N-E winter SAT anomaly (supported by Figs. 11 and 12). These processes are illustrated with October near-future I-E anomaly maps in Fig. 12. With pond scheme I used instead of E, reduced ocean heat uptake (see Fig. 11) and earlier fall freeze-up (see Fig. 5) reduce ocean-to-atmosphere upward heat flux, reducing longwave flux from July to October, latent heat flux from August to December, and sensible heat flux from November to February, ultimately reducing autumn and

winter SATs. As outlined in section 2, snow has a greater albedo than bare ice, which has a greater albedo than ponds. The pan-Arctic snow mass, and snow depth on each sea ice category, are similar between simulations of the same time period with schemes E and I. For each time period, the amount of snow at the beginning of the melt season is comparable and all snow melts by July for all simulations. We note, for the near-future simulations with scheme E instead of scheme I, slightly lower snow amounts from September through June (which may also contribute to reduced albedo). This is likely linked to the higher SATs.

KEY POINTS

For all climate periods, but with different magnitudes, removing melt ponds leads to the following:

1) Reduced absorption of SW radiation during the summer months and reduced SSTs over the summer and, as a consequence,

2) Increased sea ice cover and reduced heat flux from ocean to atmosphere over the autumn and winter, and thus

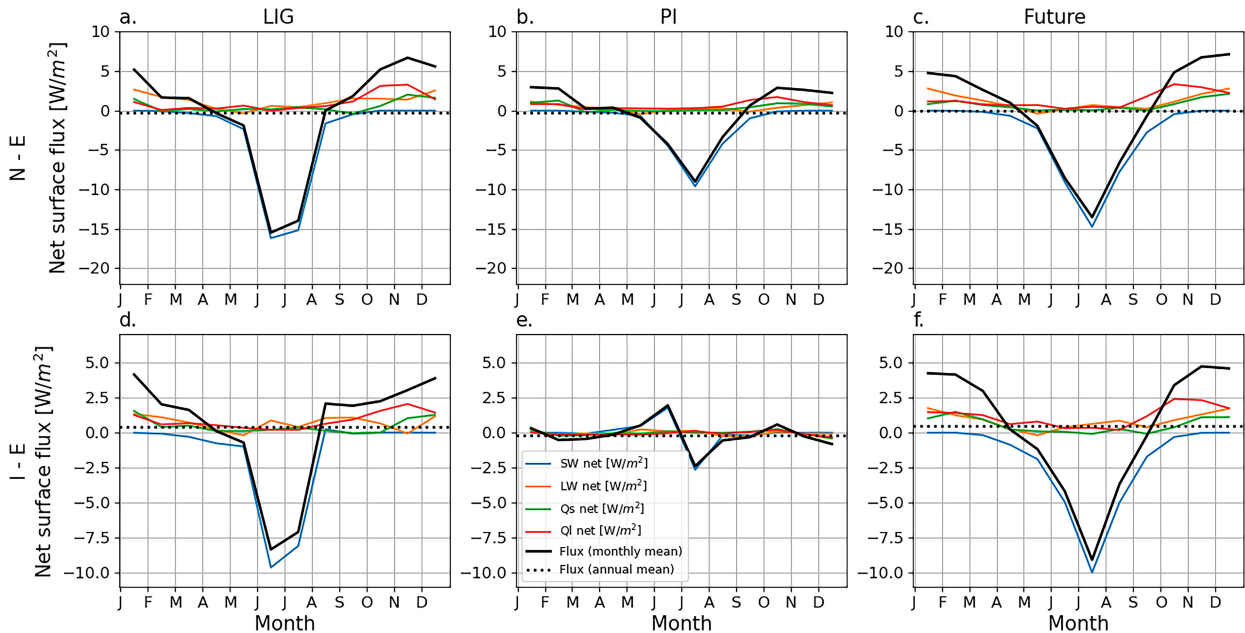3) Significantly reduced surface air temperatures in the winter.

FIG. 9. Anomaly of the long-term mean of Arctic downward surface flux from simulations with pond scheme E, showing the (a)–(c) N-E anomaly and (d)–(f) I-E anomaly for the (left) LIG, (center) PI, and (right) near-future forcings. The net monthly anomaly is shown in black and is broken down into net flux anomaly components: shortwave (blue), longwave (orange), sensible heat (green), and latent heat (red). The annual mean I-E anomaly is also shown (horizontal black dotted line).

For the PI, using pond scheme I instead of pond scheme E barely affects the summer surface energy budget, surface temperatures, and sea ice. However, for the warm climates, replacing pond scheme E with pond scheme I yields large differences in sea ice behavior, surface energy balance, and ocean and atmosphere temperatures. This is because, for the warm climates, replacing scheme E with scheme I has similar but smaller-magnitude impacts to replacing scheme E with scheme N: both replacements yield reduced summer SW surface absorption, and, in autumn and winter, increased sea ice cover and reduced heat flux and surface air temperatures (as described in points 1–3 above).

4. Conclusions

Our study spells out that Arctic sea ice and climate are strongly sensitive to melt ponds and albedo changes. This is supported by previous model studies (Flocco et al. 2010, 2012; Hunke et al. 2013; Tsamados et al. 2015), which deactivate the pond scheme entirely in standalone sea ice and coupled ice–ocean models to show that pond formation leads to significant sea ice loss. We demonstrate that the sensitivity of ice and climate to pond formation is significantly greater under warmer climate conditions—both for conditions with increased longwave forcing [in agreement with Holland et al. (2012) and Roeckner et al. (2012)] and with increased shortwave forcing [as suggested by Diamond et al. (2021)].

Additionally, we investigate the impacts on sea ice and climate of applying mechanistically different pond schemes. Scheme I is an example of an implicit "albedo tuning" method, where ponds are accounted for implicitly by reducing

the sea ice albedo linearly when the ice surface approaches its melting temperature. Scheme E is an example of a more complex "explicit" topographical scheme, where, in each grid cell, pond fraction and depth on each ice thickness category are calculated by distributing meltwater among the ice thickness categories. Implicit and explicit schemes are seen as standard, equally valid treatments of melt ponds and commonly used in many GCMs (e.g., Ridley et al. 2018b; Bailey et al. 2020; Rousset et al. 2015; Wang et al. 2016). Therefore, the same GCM with either scheme applied might be expected to give roughly equivalent results under all climate conditions—in particular, for near-present-day conditions, and, it might be hoped, for future conditions, which would bolster our faith in projections of future sea ice conditions.

However, we show that both sea ice and climate simulated by a GCM can be highly sensitive to the physics of the melt-pond treatment, by comparing results with an explicit scheme (scheme E) with those simulated with an implicit scheme (scheme I). In the PI simulations, September SIE is similar between schemes I (SIE: 7.3 ± 1.1 million km^2) and E (7.2 ± 1.0 million km^2). By contrast, under "warm-climate" conditions, replacing pond scheme E with pond scheme I yields consistently greater September SIE: 0.8 million km^2 greater under LIG and 2.6 million km^2 greater under near-future conditions. For the LIG, using scheme E leads to an ice-free September Arctic for 98% of 100 years, whereas scheme I only leads to an ice-free Arctic for 56% of 100 years. For near-future conditions, scheme E leads to an ice-free Arctic for 35% of 100 years, whereas scheme I never leads to an ice-free Arctic for these 100 years.
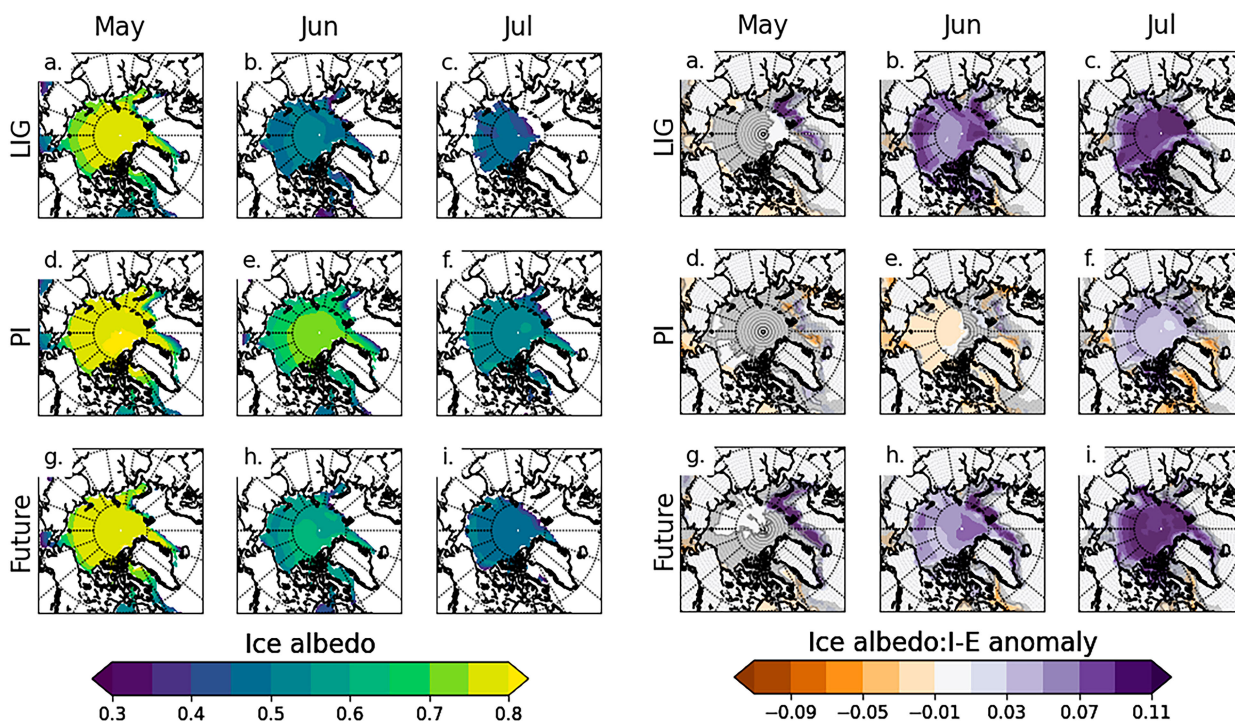
FIG. 10. Monthly maps of the long-term mean of (left) mean monthly sea ice albedo in simulations with pond scheme E and (right) monthly mean sea ice albedo anomaly for simulations with scheme I minus simulations with scheme E for (a)–(c) LIG, (d)–(f) PI, and (g)–(i) near-future conditions.

The pond scheme chosen had different impacts for each climate period because of the different sea ice state in each period: PI conditions had perennial ice cover due to thick, stable ice less sensitive to pond formation, and LIG conditions had ice so thin and sensitive that an ice-free or nearly ice-free Arctic may be simulated no matter which pond scheme is used (although the timing and duration of this near-ice-free season is controlled in part by the pond scheme chosen). By contrast, under near-future conditions, the sea ice thickness will be intermediate between the two, and thus in a state particularly sensitive to the pond scheme chosen, and magnitude of ice surface albedo changes. Therefore, in our HadGEM3 near-future simulations, sea ice was significantly thicker and more extensive with pond scheme I relative to pond scheme E.

Furthermore, we show for the first time that using mechanistically different pond schemes in a GCM (e.g., using scheme I instead of scheme E) can significantly impact simulated Northern Hemisphere air and ocean temperatures, due to inherently coupled-model behavior (ice–ocean–atmosphere interactions): under near-future conditions, using scheme E resulted in autumn Arctic surface temperatures 5° to 8°C higher than with scheme I.

These large differences to sea ice area, and air and ocean temperatures, caused by changing between implicit and explicit-type schemes, have not previously been identified in fully coupled GCMs. These large differences arise in our study due to three main factors: (i) different onset times of spring pond-related albedo reduction (scheme E ponds begin

to form in May; scheme I albedo adjustment begins later in June); (ii) different magnitudes of pond-related albedo reduction (scheme E reduces June/July ice albedo more than scheme I, leading to more June/July ice melt with scheme E); and (iii) ocean–atmosphere interactions [scheme E has reduced summer ice area and more exposed ocean, greater ocean heat uptake in summer, a warmer ocean in autumn and winter, thinner ice and greater ice surface temperatures and SATs throughout winter (as well as slightly elevated SSTs), and thinner warmer sea ice, leading to greater sensitivity to melting in the spring].

Previous studies that change between different physically based treatments of ponds in standalone sea ice models, or coupled ice–ocean models, generally yield much smaller differences to the sea ice state than those reported here for fully coupled ice–ocean–atmosphere model HadGEM3 (Flocco et al. 2010, 2012; Hunke et al. 2013; Tsamados et al. 2015; Sterlin et al. 2021; Uotila et al. 2012). This is likely because, with externally forced standalone sea ice models (or sea ice models coupled to a simple slab or mixed-layer ocean), factor (ii) above to some extent, and possibly factor (i), may occur. However, factor (iii) involves several separate feedbacks that can only be represented with a fully coupled ocean–ice–atmosphere model (or possibly, we hypothesize, an ice–ocean model coupled to a few layers of atmosphere). Pond formation strengthens the Arctic albedo feedback (Rösel and Kaleschke 2012; Eicken et al. 2004; Perovich and Tucker 1997; Curry et al. 1995). Furthermore, our results show increasing
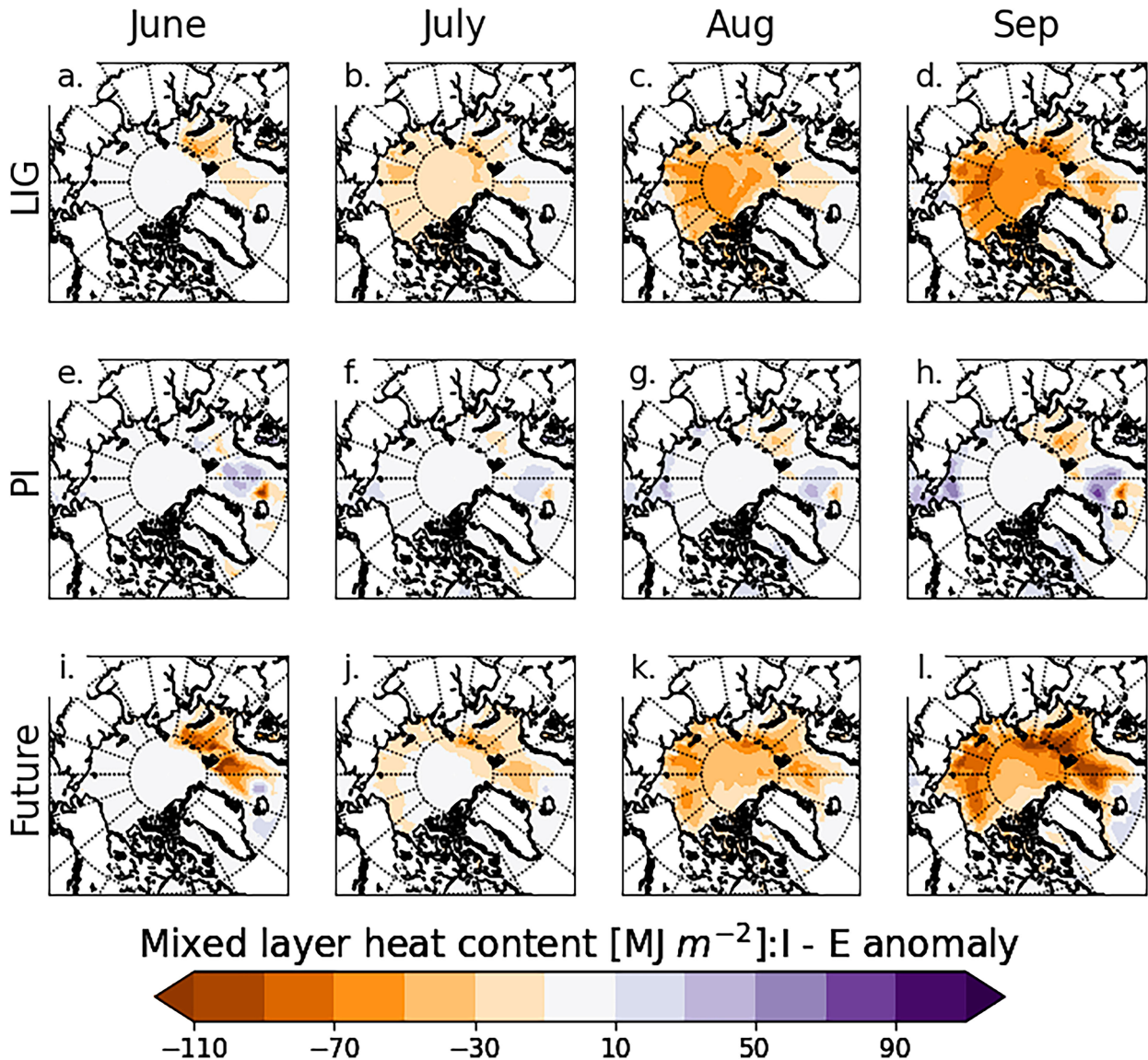
FIG. 11. Maps of the monthly anomaly of heat content in the mixed layer in simulations with pond scheme I from simulations with pond scheme E, calculated as described in section 2d, for the (a)–(d) LIG, (e)–(h) PI, and (i)–(l) near-future conditions.

magnitude with time of May to September I-E differences in SIA, open water area, ice albedo, SSTs, and ocean mixed layer heat content. Therefore, it is extremely likely that scheme E yields stronger albedo feedbacks under warm-climate conditions than scheme I, contributing to the large I-E differences in September sea ice.

Of previous studies focused on the impacts of the pond scheme, most compare results using an implicit formulation based on the one used in CCSM3 (Collins et al. 2006) (similar to scheme I), an explicit topographical scheme based on the Flocco et al. (2012) scheme (similar to scheme E), an explicit scheme based on the "level-ponds" formulation of Hunke et al. (2013), and/or a "semiempirical" treatment of ponds based on Holland et al. (2012), which is intermediate in complexity between "implicit" and the other two "explicit"-type schemes. It is difficult to perform an intercomparison, because not all studies report the same sea ice quantities or are forced by the same data, but we here present some examples:

1) Flocco et al. (2012) use a standalone sea ice model (CICE), forced by 1990–2007 atmospheric reanalysis and climatological ocean model data. They report <0.4 million km² reduction in September SIE with an explicit topographical scheme instead of an implicit scheme. They also report similar September SIE with the topographical and the semiempirical scheme.

2) Hunke et al. (2013) use CICE forced by 1980–2007 atmospheric reanalysis and climatological ocean model data. They report similar sea ice with the explicit level-ponds
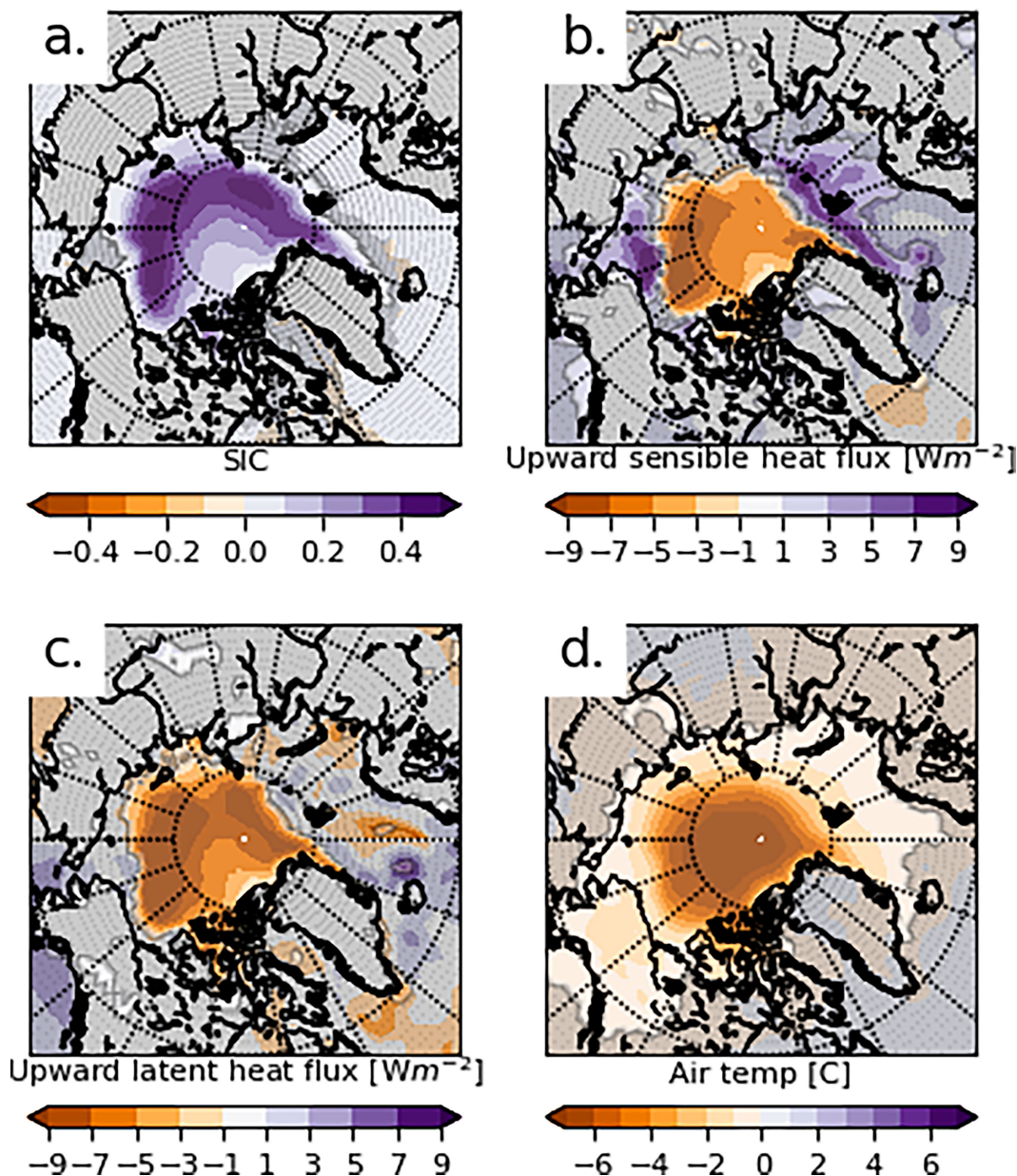
FIG. 12. Maps of the October anomaly of the long-term mean in near-future simulation with pond scheme I from near-future simulation with pond scheme E, for (a) sea ice concentration, (b) surface upward latent heat flux, (c) surface upward sensible heat flux, and (d) surface air temperature.

scheme, instead of a semiempirical scheme (September mean ice thickness difference < 0.1 m).

3) Sterlin et al. (2021) use a coupled ice–ocean model (NEMO-LIM), forced by 1958–2015 atmospheric reanalysis data. They report less than a 0.5 million km² difference in September SIE with a semiempirical scheme instead of an explicit topographical scheme.

We are aware of just one previous study that investigated the impacts on sea ice in a fully coupled ice–ocean–atmosphere model of using different physically based pond schemes. Pedersen

et al. (2009) ran ECHAM5 under PI conditions using both an implicit temperature-dependent scheme, and a semiempirical pond scheme [this applied a simpler parameterization of ponds than both scheme E and the level-ponds scheme of Hunke et al. (2013)]. September SIA was ~0.5 million km² lower with the semiempirical scheme (although September SIV was reduced by $\sim 2.5 \times 10^3$ km³, comparable to the SIV changes we find here). The focus of the study was implementing the semiempirical scheme into ECHAM5 and looking at the impacts of the scheme on simulated sea ice and surface albedo; the atmosphere and ocean response was outside its scope. Therefore, ours is the first

study to demonstrate that using two physically based, but mechanistically different, pond schemes in a GCM can lead to large (up to 2.9 million km^2) differences in simulated SIA and SIE, and air and ocean temperatures, particularly for warm past climates and for near-future projections.

Because of melt ponds' role in the ice–albedo feedback, they are important for polar amplification and climate sensitivity (Holland et al. 2012; Pithan and Mauritsen 2014; Polashenski et al. 2012; Eicken et al. 2004). It is outside the scope of this study to directly measure climate sensitivity of HadGEM3 using each different melt-pond treatment. However, given the very different sea ice and temperatures (e.g., increased air temperatures of 5°–8°C at high latitudes) simulated within 5 years when switching between treatments, it is likely that the explicit scheme significantly contributes to the 1.5× stronger albedo feedback in HadGEM3 relative to the previous version of the model (Flynn and Mauritsen 2020), as well as HadGEM3's relatively early projected ice-free Arctic date when compared with other CMIP6 models (Guarino et al. 2020). The surface albedo feedback is an important contributor to the climate sensitivity, particularly at high latitudes (Pithan and Mauritsen 2014; Hall 2004). Therefore, our study suggests the treatment of melt ponds in a GCM can strongly impact its climate sensitivity, and thus future projections of climate change.

Additionally, Guarino et al. (2020) and Vermassen et al. (2023) have recently argued that the Arctic was likely ice-free in summer during the LIG. It is important that we understand why HadGEM3 is one of the very few GCMs that appears to accurately simulate LIG Arctic sea ice and temperatures. Thus, we here have carefully, and for the first time, quantified the importance of one key model scheme, the melt pond scheme, and shown that it directly leads to the simulated ice-free Arctic for this time period.

Our simulations identify the impact of the explicit pond scheme, but do not necessarily show this scheme is more realistic. Indeed, the albedo reduction in the current setup of pond scheme E might be too strong: for example, for the LIG, Guarino et al. (2020) and Vermassen et al. (2023) provide evidence for a seasonally ice-free Arctic, but Sime et al. (2023) and Kageyama et al. (2021) suggest the LIG likely had perennial Arctic ice cover, and seasonal ice cover only occasionally. Thus, scheme E may result in overestimation of sea ice loss under warm climate conditions, while scheme I likely results in underestimation. Furthermore, Webster et al. (2022) use ground and satellite validation of pond coverage to suggest that some types of explicit schemes overestimate present-day ponding (although scheme E as used here was not included in this study). Additionally, one reason that scheme E results in large sea ice loss under warm climate conditions is due to ponds forming almost entirely on the two thinnest ice categories, which are also both the most sensitive to melting. Resultant loss of the thinnest two categories (particularly at the sea ice edge, where the ice is warmest and thinnest; see Fig. 5) can then result in melt of the remaining three categories through ocean warming. The five (or sometimes four) ice thickness categories used in GCMs are an approximation of the continuous thickness distribution of real sea ice, and recent

research by Moreno-Chamarro et al. (2020) has suggested that this approximation may be insufficient. Therefore, future model studies could usefully investigate whether the sensitivity of ice to pond-related processes under warm climate conditions is reduced if the number of ice categories is increased. We also suggest that, to test and improve the accuracy of explicit-type schemes, useful future directions include updating and improving observations of ice thickness distribution, the onset of pond formation, and pond areas and depths throughout melt season, as well as pond drainage rate through ice and off floe edges. This is particularly important, given that all these quantities could be affected by the Arctic warming, the thinning of Arctic ice, and increasing marginal ice (Falk-Petersen et al. 2000; Barber et al. 2015).

We have shown that changes to the parameterization of ponds in the sea ice submodel of a GCM can yield very large differences in simulated sea ice and climate, due to ice–ocean–atmosphere interactions. This highlights the question of how best to test our sea ice parameterizations. It suggests a need for further work to ensure that parameterizations are accurate under warm climate conditions: some studies (e.g., Roach et al. 2018) suggest that poorly known parameters may be modified to fit present-day modeling needs. However, we have shown here that sea ice parameterizations that yield approximately equivalent results under the preindustrial climate do not necessarily give similar results under other climate conditions—for example, near-future and palaeoclimate conditions. This is of concern for climate modelers as the model setup is only tuned for one climate state [see also Hopcroft and Valdes (2015), who reached similar conclusions when considering the Last Glacial Maximum and preindustrial climate, but focusing on vegetation rather than sea ice]. Thus, further work on sea ice processes is crucial to more confidently predict sea ice cover change over the coming decades.

Through this study, we have isolated the impact of a key component of the sea ice model (the melt pond scheme) on climate simulations for different climate states. We have shown that use of mechanistically different pond schemes can strongly impact not only sea ice, but also ocean and atmospheric conditions through the surface energy balance. In particular, our "future climate" setup showed a high sensitivity to the type of pond scheme used: a change of pond scheme made the difference between seasonal and perennial Arctic sea ice cover, and resulted in air temperature differences of up to 5°–8°C at high latitudes. This has implications for CMIP future scenario runs, as different CMIP6 models use several mechanistically different treatments of ponds. Our focus on melt ponds has demonstrated their importance and wider impacts on the ocean and atmosphere (Perovich et al. 2007a,b; Flocco et al. 2012; Taylor and Feltham 2004; Lüthje et al. 2006; Skyllingstad et al. 2009; Scott and Feltham 2010; Flocco et al. 2012). Because of the contribution of melt ponds to the sea ice albedo feedback they affect polar amplification and climate sensitivity (Holland et al. 2012; Pithan and Mauritsen 2014; Polashenski et al. 2012; Eicken et al. 2004). Therefore, in our models, improving and better evaluating the representation of sea ice processes, and particularly melt ponds, is vital for robust projections of future climate change.

Data availability statement. The HadGEM3 model outputs prepared for CMIP6, including the simulated PI, are in the ESGF archive (https://doi.org/10.22033/ESGF/CMIP6.419; Ridley et al. 2018a). Processed and additional HadGEM3 model outputs used in this study are available online (http://gws-access.jasmin.ac.uk/public/pmip4/JClim_Diamondetal_2022). The authors declare that all other data are available in the paper and the online supplemental material.

REFERENCES

Andrews, M. B., and Coauthors, 2020: Historical simulations with HadGEM3-GC3.1 for CMIP6. *J. Adv. Model. Earth Syst.*, **12**, e2019MS001995, https://doi.org/10.1029/2019MS001995.

Andrews, T., and Coauthors, 2019: Forcings, feedbacks, and climate sensitivity in HadGEM3-GC3.1 and UKESM1. *J. Adv. Model. Earth Syst.*, **11**, 4377–4394, https://doi.org/10.1029/2019MS001866.

Bailey, D. A., M. M. Holland, A. K. DuVivier, E. C. Hunke, and A. K. Turner, 2020: Impact of a new sea ice thermodynamic formulation in the CESM2 sea ice component. *J. Adv. Model. Earth Syst.*, **12**, e2020MS002154, https://doi.org/10.1029/2020MS002154.

Barber, D. G., and Coauthors, 2015: Selected physical, biological and biogeochemical implications of a rapidly changing Arctic marginal ice zone. *Prog. Oceanogr.*, **139**, 122–150, https://doi.org/10.1016/j.pocean.2015.09.003.

Bateson, A. W., D. L. Feltham, D. Schröder, Y. Wang, B. Hwang, J. K. Ridley, and Y. Aksenov, 2022: Sea ice floe size: Its impact on pan-Arctic and local ice mass and required model complexity. *Cryosphere*, **16**, 2565–2593, https://doi.org/10.5194/tc-16-2565-2022.

Berger, A., and M.-F. Loutre, 1991: Insolation values for the climate of the last 10 million years. *Quat. Sci. Rev.*, **10**, 297–317, https://doi.org/10.1016/0277-3791(91)90033-Q.

Bitz, C. M., and W. H. Lipscomb, 1999: An energy-conserving thermodynamic model of sea ice. *J. Geophys. Res.*, **104**, 15 669–15 677, https://doi.org/10.1029/1999JC900100.

Collins, W. D., and Coauthors, 2006: The Community Climate System Model version 3 (CCSM3). *J. Climate*, **19**, 2122–2143, https://doi.org/10.1175/JCLI3761.1.

Curry, J. A., J. L. Schramm, and E. E. Ebert, 1995: Sea ice-albedo climate feedback mechanism. *J. Climate*, **8**, 240–247, https://doi.org/10.1175/1520-0442(1995)008<0240:SIACFM>2.0.CO;2.

——, ——, D. K. Perovich, and J. O. Pinto, 2001: Applications of SHEBA/FIRE data to evaluation of snow/ice albedo parameterizations. *J. Geophys. Res.*, **106**, 15 345–15 355, https://doi.org/10.1029/2000JD900311.

Diamond, R., L. C. Sime, D. Schroeder, and M.-V. Guarino, 2021: The contribution of melt ponds to enhanced Arctic sea-ice melt during the last interglacial. *Cryosphere*, **15**, 5099–5114, https://doi.org/10.5194/tc-15-5099-2021.

Docquier, D., and T. Koenigk, 2021: Observation-based selection of climate models projects Arctic ice-free summers around 2035. *Commun. Earth Environ.*, **2**, 144, https://doi.org/10.1038/s43247-021-00214-7.

Eicken, H., T. C. Grenfell, D. K. Perovich, J. A. Richter-Menge, and K. Frey, 2004: Hydraulic controls of summer Arctic pack ice albedo. *J. Geophys. Res.*, **109**, C08007, https://doi.org/10.1029/2003JC001989.

Eyring, V., S. Bony, G. A. Meehl, C. A. Senior, B. Stevens, R. J. Stouffer, and K. E. Taylor, 2016: Overview of the Coupled Model Intercomparison Project phase 6 (CMIP6) experimental design and organization. *Geosci. Model Dev.*, **9**, 1937–1958, https://doi.org/10.5194/gmd-9-1937-2016.

Falk-Petersen, S., and Coauthors, 2000: Physical and ecological processes in the marginal ice zone of the northern Barents Sea during the summer melt period. *J. Mar. Syst.*, **27**, 131–159, https://doi.org/10.1016/S0924-7963(00)00064-6.

Fetterer, F., and N. Untersteiner, 1998: Observations of melt ponds on Arctic sea ice. *J. Geophys. Res.*, **103**, 24 821–24 835, https://doi.org/10.1029/98JC02034.

Flocco, D., and D. L. Feltham, 2007: A continuum model of melt pond evolution on Arctic sea ice. *J. Geophys. Res.*, **112**, C08016, https://doi.org/10.1029/2006JC003836.

——, ——, and A. K. Turner, 2010: Incorporation of a physically based melt pond scheme into the sea ice component of a climate model. *J. Geophys. Res.*, **115**, C08012, https://doi.org/10.1029/2009JC005568.

——, D. Schroeder, D. L. Feltham, and E. C. Hunke, 2012: Impact of melt ponds on Arctic sea ice simulations from 1990 to 2007. *J. Geophys. Res.*, **117**, C09032, https://doi.org/10.1029/2012JC008195.

Flynn, C. M., and T. Mauritsen, 2020: On the climate sensitivity and historical warming evolution in recent coupled model ensembles. *Atmos. Chem. Phys.*, **20**, 7829–7842, https://doi.org/10.5194/acp-20-7829-2020.

Guarino, M.-V., and Coauthors, 2020: Sea-ice-free Arctic during the last interglacial supports fast future loss. *Nat. Climate Change*, **10**, 928–932, https://doi.org/10.1038/s41558-020-0865-2.

——, L. C. Sime, R. Diamond, J. Ridley, and D. Schroeder, 2023: The coupled system response to 250 years of freshwater forcing: Last interglacial CMIP6–PMIP4 HadGEM3 simulations. *Climate Past*, **19**, 865–881, https://doi.org/10.5194/cp-19-865-2023.

Hall, A., 2004: The role of surface albedo feedback in climate. *J. Climate*, **17**, 1550–1568, https://doi.org/10.1175/1520-0442(2004)017<1550:TROSAF>2.0.CO;2.

Holland, M. M., D. A. Bailey, B. P. Briegleb, B. Light, and E. Hunke, 2012: Improved sea ice shortwave radiation physics in CCSM4: The impact of melt ponds and aerosols on Arctic sea ice. *J. Climate*, **25**, 1413–1430, https://doi.org/10.1175/JCLI-D-11-00078.1.

Hopcroft, P. O., and P. J. Valdes, 2015: Last glacial maximum constraints on the Earth system model HadGEM2-ES. *Climate Dyn.*, **45**, 1657–1672, https://doi.org/10.1007/s00382-014-2421-0.

Hunke, E. C., and W. H. Lipscomb, 2010: CICE: The Los Alamos Sea ice model documentation and software user's manual, version 4.1. Doc. LA-CC-06-012, 76 pp., http://csdms.colorado.edu/w/images/CICE_documentation_and_software_user's_manual.pdf.

——, D. A. Hebert, and O. Lecomte, 2013: Level-ice melt ponds in the Los Alamos sea ice model, CICE. *Ocean Modell.*, **71**, 26–42, https://doi.org/10.1016/j.ocemod.2012.11.008.

——, W. H. Lipscomb, A. K. Turner, N. Jeffery, and S. Elliott, 2015: CICE: The Los Alamos Sea ice model documentation and software user's manual, version 5.1. Doc. LA-CC-06-012, 116 pp., https://svn-ccsm-models.cgd.ucar.edu/cesm1/alphas/branches/cesm1_5_alpha04c_timers/components/cice/src/doc/cicedoc.pdf.

Jackson, L. C., R. Kahana, T. Graham, M. A. Ringer, T. Woollings, J. V. Mecking, and R. A. Wood, 2015: Global and European climate impacts of a slowdown of the AMOC in a high resolution GCM. *Climate Dyn.*, **45**, 3299–3316, https://doi.org/10.1007/s00382-015-2540-2.

Jahn, A., J. E. Kay, M. M. Holland, and D. M. Hall, 2016: How predictable is the timing of a summer ice-free Arctic? *Geophys. Res. Lett.*, **43**, 9113–9120, https://doi.org/10.1002/2016GL070067.

Kageyama, M., and Coauthors, 2021: A multi-model CMIP6-PMIP4 study of Arctic sea ice at 127 ka: Sea ice data compilation and model differences. *Climate Past*, **17**, 37–62, https://doi.org/10.5194/cp-17-37-2021.

Lüthje, M., D. L. Feltham, P. D. Taylor, and M. G. Worster, 2006: Modeling the summertime evolution of sea-ice melt ponds. *J. Geophys. Res.*, **111**, C02001, https://doi.org/10.1029/2004JC002818.

Madec, G., and Coauthors, 2015: Nemo ocean engine, version 3.6. Note du Pôle de modéllisation de l'Institut Pierre-Simon Laplace No 27, 401 pp., https://epic.awi.de/id/eprint/39698/1/NEMO_book_v6039.pdf.

Massonnet, F., T. Fichefet, H. Goosse, C. M. Bitz, G. Philippon-Berthier, M. M. Holland, and P.-Y. Barriat, 2012: Constraining projections of summer Arctic sea ice. *Cryosphere*, **6**, 1383–1394, https://doi.org/10.5194/tc-6-1383-2012.

Meehl, G. A., C. A. Senior, V. Eyring, G. Flato, J.-F. Lamarque, R. J. Stouffer, K. E. Taylor, and M. Schlund, 2020: Context for interpreting equilibrium climate sensitivity and transient climate response from the CMIP6 Earth system models. *Sci. Adv.*, **6**, eaba1981, https://doi.org/10.1126/sciadv.%20aba1981.

Meier, W., F. Fetterer, A. Windnagel, and J. Stewart, 2021: NOAA/NSIDC climate data record of passive microwave sea ice concentration, version 4. National Snow and Ice Data Center, accessed July 2022, https://doi.org/10.7265/efmz-2t65.

Menary, M. B., and Coauthors, 2018: Preindustrial control simulations with HadGEM3-GC3.1 for CMIP6. *J. Adv. Model. Earth Syst.*, **10**, 3049–3075, https://doi.org/10.1029/2018MS001495.

Moreno-Chamarro, E., P. Ortega, and F. Massonnet, 2020: Impact of the ice thickness distribution discretization on the sea ice concentration variability in the NEMO3.6–LIM3 global ocean–sea ice model. *Geosci. Model Dev.*, **13**, 4773–4787, https://doi.org/10.5194/gmd-13-4773-2020.

Notz, D., and J. Stroeve, 2016: Observed Arctic sea-ice loss directly follows anthropogenic CO_2 emission. *Science*, **354**, 747–750, https://doi.org/10.1126/science.aag2345.

——, and ——, 2018: The trajectory towards a seasonally ice-free Arctic Ocean. *Curr. Climate Change Rep.*, **4**, 407–416, https://doi.org/10.1007/s40641-018-0113-2.

——, and SIMIP Community, 2020: Arctic sea ice in CMIP6. *Geophys. Res. Lett.*, **47**, e2019GL086749, https://doi.org/10.1029/2019GL086749.

Otto-Bliesner, B. L., and Coauthors, 2017: The PMIP4 contribution to CMIP6–Part 2: Two interglacials, scientific objective and experimental design for Holocene and last interglacial simulations. *Geosci. Model Dev.*, **10**, 3979–4003, https://doi.org/10.5194/gmd-10-3979-2017.

Pedersen, C. A., E. Roeckner, M. Lüthje, and J.-G. Winther, 2009: A new sea ice albedo scheme including melt ponds for ECHAM5 general circulation model. *J. Geophys. Res.*, **114**, D08101, https://doi.org/10.1029/2008JD010440.

Perovich, D. K., and W. B. Tucker III, 1997: Arctic sea-ice conditions and the distribution of solar radiation during summer. *Ann. Glaciol.*, **25**, 445–450, https://doi.org/10.3189/S0260305500014439.

——, T. C. Grenfell, B. Light, and P. V. Hobbs, 2002a: Seasonal evolution of the albedo of multiyear Arctic sea ice. *J. Geophys. Res.*, **107**, 8044, https://doi.org/10.1029/2000JC000438.

——, W. B. Tucker III, and K. A. Ligett, 2002b: Aerial observations of the evolution of ice surface conditions during summer. *J. Geophys. Res.*, **107**, 8048, https://doi.org/10.1029/2000JC000449.

——, B. Light, H. Eicken, K. F. Jones, K. Runciman, and S. V. Nghiem, 2007a: Increasing solar heating of the Arctic Ocean and adjacent seas, 1979–2005: Attribution and role in the ice-albedo feedback. *Geophys. Res. Lett.*, **34**, L19505, https://doi.org/10.1029/2007GL031480.

——, S. V. Nghiem, T. Markus, and A. Schweiger, 2007b: Seasonal evolution and interannual variability of the local solar energy absorbed by the Arctic sea ice–ocean system. *J. Geophys. Res.*, **112**, C03005, https://doi.org/10.1029/2006JC003558.

Pithan, F., and T. Mauritsen, 2014: Arctic amplification dominated by temperature feedbacks in contemporary climate models. *Nat. Geosci.*, **7**, 181–184, https://doi.org/10.1038/ngeo2071.

Polashenski, C., D. Perovich, and Z. Courville, 2012: The mechanisms of sea ice melt pond formation and evolution. *J. Geophys. Res.*, **117**, C01001, https://doi.org/10.1029/2011JC007231.

Post, E., and Coauthors, 2013: Ecological consequences of sea-ice decline. *Science*, **341**, 519–524, https://doi.org/10.1126/science.1235225.

Rae, J. G. L., H. T. Hewitt, A. B. Keen, J. K. Ridley, J. M. Edwards, and C. M. Harris, 2014: A sensitivity study of the sea ice simulation in the global coupled climate model, HadGEM3. *Ocean Modell.*, **74**, 60–76, https://doi.org/10.1016/j.ocemod.2013.12.003.

——, ——, ——, ——, A. E. West, C. M. Harris, E. C. Hunke, and D. N. Walters, 2015: Development of the global sea ice 6.0 CICE configuration for the Met Office global coupled model. *Geosci. Model Dev.*, **8**, 2221–2230, https://doi.org/10.5194/gmd-8-2221-2015.

Ridley, J. K., M. Menary, T. Kuhlbrodt, M. Andrews, and T. Andrews, 2018a: MOHC HadGEM3-GC31-LL model output prepared for CMIP6 CMIP. Earth System Grid Federation, accessed May 2022, https://doi.org/10.22033/ESGF/CMIP6.419.

——, E. W. Blockley, A. B. Keen, J. G. L. Rae, A. E. West, and D. Schroeder, 2018b: The sea ice model component of HadGEM3-GC3.1. *Geosci. Model Dev.*, **11**, 713–723, https://doi.org/10.5194/gmd-11-713-2018.

Roach, L. A., S. F. B. Tett, M. J. Mineter, K. Yamazaki, and C. D. Rae, 2018: Automated parameter tuning applied to sea ice in a global climate model. *Climate Dyn.*, **50**, 51–65, https://doi.org/10.1007/s00382-017-3581-5.

Roeckner, E., T. Mauritsen, M. Esch, and R. Brokopf, 2012: Impact of melt ponds on Arctic sea ice in past and future climates as simulated by MPI-ESM. *J. Adv. Model. Earth Syst.*, **4**, M00A02, https://doi.org/10.1029/2012MS000157.

Rösel, A., and L. Kaleschke, 2012: Exceptional melt pond occurrence in the years 2007 and 2011 on the Arctic sea ice revealed from MODIS satellite data. *J. Geophys. Res.*, **117**, C05018, https://doi.org/10.1029/2011JC007869.

Rosenblum, E., and I. Eisenman, 2017: Sea ice trends in climate models only accurate in runs with biased global warming. *J. Climate*, **30**, 6265–6278, https://doi.org/10.1175/JCLI-D-16-0455.1.

Rousset, C., and Coauthors, 2015: The Louvain-La-Neuve sea ice model LIM3.6: Global and regional capabilities. *Geosci. Model Dev.*, **8**, 2991–3005, https://doi.org/10.5194/gmd-8-2991-2015.

Schmidtko, S., G. C. Johnson, and J. M. Lyman, 2013: MIMOC: A global monthly isopycnal upper-ocean climatology with mixed layers. *J. Geophys. Res. Oceans*, **118**, 1658–1672, https://doi.org/10.1002/jgrc.20122.

Schröder, D., and W. M. Connolley, 2007: Impact of instantaneous sea ice removal in a coupled general circulation model. *Geophys. Res. Lett.*, **34**, L14502, https://doi.org/10.1029/2007GL030253.

——, D. L. Feltham, D. Flocco, and M. Tsamados, 2014: September Arctic sea-ice minimum predicted by spring melt-pond fraction. *Nat. Climate Change*, **4**, 353–357, https://doi.org/10.1038/nclimate2203.

Scott, F., and D. L. Feltham, 2010: A model of the three-dimensional evolution of Arctic melt ponds on first-year and multiyear sea ice. *J. Geophys. Res.*, **115**, C12064, https://doi.org/10.1029/2010JC006156.

Sévellec, F., A. V. Fedorov, and W. Liu, 2017: Arctic sea-ice decline weakens the Atlantic meridional overturning circulation. *Nat. Climate Change*, **7**, 604–610, https://doi.org/10.1038/nclimate3353.

Sime, L. C., R. Sivankutty, I. Vallet-Malmierca, A. M. de Boer, and M. Sicard, 2023: Summer surface air temperature proxies point to near sea-ice-free conditions in the Arctic at 127 ka. *Climate Past*, **19**, 883–900, https://doi.org/10.5194/cp-19-883-2023.

Skyllingstad, E. D., C. A. Paulson, and D. K. Perovich, 2009: Simulation of melt pond evolution on level ice. *J. Geophys. Res.*, **114**, C12019, https://doi.org/10.1029/2009JC005363.

Sterlin, J., T. Fichefet, F. Massonnet, O. Lecomte, and M. Vancoppenolle, 2021: Sensitivity of Arctic sea ice to melt pond processes and atmospheric forcing: A model study. *Ocean Modell.*, **167**, 101872, https://doi.org/10.1016/j.ocemod.2021.101872.

Taylor, P. D., and D. L. Feltham, 2004: A model of melt pond evolution on sea ice. *J. Geophys. Res.*, **109**, C12007, https://doi.org/10.1029/2004JC002361.

Tsamados, M., D. Feltham, A. Petty, D. Schroeder, and D. Flocco, 2015: Processes controlling surface, bottom and lateral melt of Arctic sea ice in a state of the art sea ice model. *Philos. Trans. Roy. Soc.*, **373A**, 20140167, https://doi.org/10.1098/rsta.2014.0167.

Uotila, P., S. O'Farrell, S. J. Marsland, and D. Bi, 2012: A sea-ice sensitivity study with a global ocean-ice model. *Ocean Modell.*, **51**, 1–18, https://doi.org/10.1016/j.ocemod.2012.04.002.

Vermassen, F., and Coauthors, 2023: A seasonally ice-free Arctic ocean during the last interglacial. *Nat. Geosci.*, **16**, 723–729, https://doi.org/10.1038/s41561-023-01227-x.

Vihma, T., 2014: Effects of Arctic sea ice decline on weather and climate: A review. *Surv. Geophys.*, **35**, 1175–1214, https://doi.org/10.1007/s10712-014-9284-0.

Walters, D., and Coauthors, 2017: The Met Office Unified Model global atmosphere 6.0/6.1 and JULES global land 6.0/6.1 configurations. *Geosci. Model Dev.*, **10**, 1487–1520, https://doi.org/10.5194/gmd-10-1487-2017.

Wang, Q., and Coauthors, 2016: An assessment of the Arctic Ocean in a suite of interannual CORE-II simulations. Part I: Sea ice and solid freshwater. *Ocean Modell.*, **99**, 110–132, https://doi.org/10.1016/j.ocemod.2015.12.008.

Webster, M. A., and Coauthors, 2022: Spatiotemporal evolution of melt ponds on Arctic sea ice: MOSAIC observations and model results. *Elementa*, **10**, 000072, https://doi.org/10.1525/elementa.2021.000072.

West, A. E., A. J. McLaren, H. T. Hewitt, and M. J. Best, 2016: The location of the thermodynamic atmosphere–ice interface in fully coupled models—A case study using JULES and CICE. *Geosci. Model Dev.*, **9**, 1125–1141, https://doi.org/10.5194/gmd-9-1125-2016.

Williams, K. D., and Coauthors, 2018: The Met Office global coupled model 3.0 and 3.1 (GC3.0 and GC3.1) configurations. *J. Adv. Model. Earth Syst.*, **10**, 357–380, https://doi.org/10.1002/2017MS001115.